

REPORT DOCUMENTATION PAGE

Form Approved
OMB No. 0704-0188

Public reporting burden for this collection of information is estimated to average 1 hour per response, including the time for reviewing instructions, searching data sources, gathering and maintaining the data needed, and completing and reviewing the collection of information. Send comments regarding this burden estimate or any other aspect of this collection of information, including suggestions for reducing this burden to Washington Headquarters Service, Directorate for Information Operations and Reports, Paperwork Reduction Project (0704-0188) Washington DC 20503
PLEASE DO NOT RETURN YOUR FORM TO THE ABOVE ADDRESS.

1. REPORT DATE (DD-MM-YYYY) 30-03-2007		2. REPORT DATE Final Technical Rep.		3. DATES COVERED: (From - To) 01/01/04 - 21/31/06	
4. TITLE AND SUBTITLE Large Eddy Simulation for Heat Transfer Prediction in a Gas Turbine Environment: Development of a high-order overset mesh LES solver				5a. CONTRACT NUMBER FA9550-04-1-0031- XXXXXX	
				5b. GRANT NUMBER FA9550-04-1-0031- XXXXXX	
				5c. PROGRAM ELEMENT NUMBER	
6. AUTHOR(S) Sanjiva K. Lele, R. Bhaskaran and Z. Xiong				5d. PROJECT NUMBER	
				5e. TASK NUMBER	
				5f. WORK UNIT NUMBER	
7. PERFORMING ORGANIZATION NAME(S) AND ADDRESS(ES) Stanford University 651 Serra Street Stanford, CA 94305				8. PERFORMING ORGANIZATION REPORT NUMBER	
9. SPONSORING/MONITORING AGENCY NAME(S) AND ADDRESS(ES) Air Force Office of Scientific Research (AFOSR) Lt. Col. Dr. Rhett Jefferies, Program Manager 875 N. Randolph St Arlington VA 22203				10. SPONSOR/MONITOR'S ACRONYM(S) AFRL-SR-AR-TR-07-0320	
12. DISTRIBUTION AVAILABILITY STATEMENT Unclassified Unlimited					
13. SUPPLEMENTARY NOTES					
14. ABSTRACT A thorough investigation of leading edge heat transfer on a model geometry has been performed using Large-eddy simulation (LES), with support from the current and a previous AFOSR grant. The results from the leading edge study are presented as a detailed Appendix in this report. To address the problem of solving the full three-dimensional turbulent flow in a turbine passage, including the effects of free-stream turbulence from the combustor, and the unsteady interactions between various blade rows in the form of moving wakes and shocks it was necessary to extend the LES solver. A high-order overset LES code suitable for the study of turbomachinery passages has been developed. This approach is summarized in this report. Some preliminary results have been obtained using this code, mostly as cases for code validation. The code is currently being used to investigate flow in turbine passages under realistic conditions, and detailed comparisons with available experiments will be made.					
15. SUBJECT TERMS LES for Turbomachinery, Heat Transfer Prediction, Effect of Free-stream Turbulence					
16. SECURITY CLASSIFICATION OF:			17. LIMITATION OF ABSTRACT UU	18. NUMBER OF PAGES 64	19a. NAME OF RESPONSIBLE PERSON
a. REPORT UU	b. ABSTRACT UU	c. THIS PAGE UU			20b. TELEPHONE NUMBER (include area code)

Large Eddy Simulation for Heat Transfer Prediction in a Gas Turbine Environment: Development of a high-order overset mesh LES solver

Sanjiva K. Lele, Rathakrishnan Bhaskaran and Zhongmin Xiong

Department of Mechanical Engineering
Stanford University

Abstract

A thorough investigation of leading edge heat transfer on a model geometry has been performed using Large-eddy simulation (LES), with support from the current and a previous AFOSR grant. The results from the leading edge study are presented as a detailed Appendix in this report. To address the problem of solving the full three-dimensional turbulent flow in a turbine passage, including the effects of free-stream turbulence from the combustor, and the unsteady interactions between various blade rows in the form of moving wakes and shocks it was necessary to extend the LES solver. A high-order overset LES code suitable for the study of turbomachinery passages has been developed. This approach is summarized in this report. Some preliminary results have been obtained using this code, mostly as cases for code validation. The code is currently being used to investigate flow in turbine passages under realistic conditions, and detailed comparisons with available experiments will be made.

Supported by AFOSR Grant No. FA9550-04-1-0031 ~~XXXXXX~~

20070910331

1 Introduction and Objectives

The current trend in design of gas turbine engines is to achieve a reduction in cost and weight of the engine and at the same time not compromise on the thrust developed by them. There are primarily two avenues to achieve this *viz.*, (i) by using fewer blades and heavily loading them, and (ii) by increasing the turbine inlet temperature. As a result the nozzle guide vanes and rotor blades of a high-pressure turbine (HPT) are exposed to a hostile thermal environment. Active cooling of the blade surfaces becomes necessary in order to maintain their integrity. This has a performance penalty since the air required to cool the blades is bled from the compressor. The increased loading of the blades leads to boundary layer separation and results in performance losses. Therefore heat transfer prediction of the thermally critical regions and flow prediction in the blade passage are a vital elements of the overall improvement of gas turbine engines.

The primary objective of this project was to investigate fundamental issues controlling aerodynamic losses and elevated heat-transfer to turbine vane and rotor blades using large eddy simulations (LES). LES simulation methodology was used to study the physics behind simplified problems relevant to turbomachinery.

(a) Simulation of realistic free-stream turbulence with intensity and length scale appropriate for turbine blade heat-transfer and study the heat-transfer augmentation in idealized geometry and its interaction with blade leading edge region

(b) Simulation of the disturbed turbulent boundary layers over a realistic turbine blade surface (in a blade row cascade) in the presence of free-stream turbulence and combustor hot streaks and the resulting blade heat transfer distribution

Other flow processes such as blade row interactions, tip vortices, tip clearance flows, and secondary flows in the blade row that are critical to the overall predictions in a realistic turbine blade row were not considered.

A high order overset LES code was developed in order to perform numerical investigation of the

above listed problems. In the following sections, we will look at the form of the Navier-Stokes equations suitable for the problems of interest and discuss the implementation in the LES code. We will then look at some results obtained using this high order LES code.

2 Governing Equations

The equations governing the flow of a compressible Newtonian fluid obeying Fourier's law of heat conduction can be written in terms of the contravariant velocity components (v^i), in a general curvilinear coordinate system (x^i) as (Aris (1989))

$$\frac{\partial \rho}{\partial t} + (\rho v^k)_{,k} = 0 \quad (1)$$

$$\frac{\partial}{\partial t}(\rho v^i) + (\rho v^i v^j)_{,j} = - \left[\left(p + \frac{2}{3} \mu v^k_{,k} \right) g^{ij} \right]_{,j} + \left[\mu \left(g^{jk} v^i_{,k} + g^{ik} v^j_{,k} \right) \right]_{,j} \quad (2)$$

$$\frac{\partial E}{\partial t} + [(E + p)v^j]_{,j} = \left(\kappa g^{ij} T_{,i} \right)_{,j} + \left(\tau^{ij} g_{ik} v^k \right)_{,j} \quad (3)$$

where, g_{ij} and g^{ij} are the covariant and contravariant metric tensors respectively. The equations are recast in the following form to facilitate numerical implementation

$$\frac{\partial}{\partial t}(\sqrt{g}\rho) + \frac{\partial}{\partial x^k}(\sqrt{g}\rho v^k) = 0 \quad (4)$$

$$\begin{aligned} \frac{\partial}{\partial t}(\sqrt{g}\rho v^i) + \frac{\partial}{\partial x^j}(\sqrt{g}\rho v^i v^j) + \Gamma_{qj}^i \sqrt{g}\rho v^i v^j &= \frac{\partial}{\partial x^k} \left\{ \sqrt{g} \left[g^{ij} \left(p + \frac{2}{3} \mu v^k_{,k} \right) \right] \right\} \\ &+ \Gamma_{qj}^i \sqrt{g} \left[g^{ij} \left(p + \frac{2}{3} \mu v^k_{,k} \right) \right] \end{aligned} \quad (5)$$

$$\frac{\partial}{\partial t}(\sqrt{g}E) + \frac{\partial}{\partial x^j} \left[\sqrt{g}(E + p)v^j \right] = \frac{\partial}{\partial x^j} \left\{ \sqrt{g} \left[\kappa g^{ij} \frac{\partial T}{\partial x^i} + \tau^{ij} g_{ik} v^k \right] \right\} \quad (6)$$

where $J = \sqrt{g}$ is the Jacobian. Hence, a natural choice of the dependent vector variables would be $\mathbf{q} = \{\sqrt{g}\rho, \sqrt{g}\rho v^i, \sqrt{g}E\}$.

A filter $G(\mathbf{x})$ with compact support is then applied to the governing equations in the domain of interest (Ω) to derive the equations for LES. Any tensor quantity $A_{j_1 \dots j_n}^{i_1 \dots i_m}$ may be filtered as

$$\overline{\sqrt{g} A_{j_1 \dots j_n}^{i_1 \dots i_m}}(\mathbf{x}, t) = \iiint_{\Omega} A_{j_1 \dots j_n}^{i_1 \dots i_m}(\mathbf{x}', t) G(\mathbf{x} - \mathbf{x}') \sqrt{g} d\mathbf{x}'$$

The curvilinear equivalent of Favre filtering can be written as

$$\bar{A}_{j_1 \dots j_n}^{i_1 \dots i_m} = \frac{\overline{\sqrt{g} A_{j_1 \dots j_n}^{i_1 \dots i_m}}}{\sqrt{g\rho}}$$

Using this definition, we can write the filtered governing equations as

$$\frac{\partial}{\partial t}(\overline{\sqrt{g}\rho}) + \frac{\partial}{\partial x_k}(\overline{\sqrt{g}\rho v^k}) = 0 \quad (7)$$

$$\begin{aligned} \frac{\partial}{\partial t}(\overline{\sqrt{g}\rho v^i}) + \frac{\partial}{\partial x^j}(\overline{\sqrt{g}\rho v^i v^j}) + \Gamma_{qj}^i \overline{\sqrt{g}\rho v^i v^j} &= -\frac{\partial}{\partial x^j} (g^{ij} \overline{\sqrt{g}p}) - \Gamma_{qj}^i \overline{\sqrt{g}p} + \frac{\partial}{\partial x^j} (\overline{\sqrt{g}\tau^{ij}}) \\ &\quad - \frac{\partial}{\partial x^j} sgs\tau^{ij} - \Gamma_{qj}^i sgs\tau^{qj} \end{aligned} \quad (8)$$

$$\begin{aligned} \frac{\partial}{\partial t}(\overline{\sqrt{g}E}) + \frac{\partial}{\partial x^j} [\overline{\sqrt{g}(E+p)} v^j] &= -\frac{\partial}{\partial x^j} (\overline{\sqrt{g}\dot{q}^j}) + \frac{\partial}{\partial x^j} (\overline{\sqrt{g}\tau^{ij}} g_{ik} v^k) \\ &\quad - \frac{\partial}{\partial x^j} (sgs\dot{q}^j) \end{aligned} \quad (9)$$

where the resolved and sub-grid scale stress tensor and heat flux vector are

$$\bar{\tau}^{ij} = \frac{\bar{\mu}}{Re} \left(g^{jk} \bar{v}_{,k}^i + g^{ik} \bar{v}_{,k}^j - \frac{2}{3} g^{ij} \bar{v}_{,k}^k \right) \quad (10)$$

$$\bar{q}^j = -\frac{\bar{\mu}}{RePr} g^{jk} \frac{\partial \bar{T}}{\partial x^k} \quad (11)$$

$$sgs\tau^{ij} = \overline{\sqrt{g}\rho} (v^i v^j - \bar{v}^i \bar{v}^j) \quad (12)$$

$$sgs\dot{q}^j = \overline{\sqrt{g}\rho} (T v^j - \bar{T} \bar{v}^j) \quad (13)$$

In addition, the equation of state becomes

$$\overline{\sqrt{g}p} = \frac{\gamma - 1}{\gamma} \overline{\sqrt{g}\rho \bar{T}} \quad (14)$$

The resulting sub-grid scale (SGS) stress tensors are closed using the dynamic Smagorinsky model (See Nagarajan (2004) for the details).

3 Numerical Implementation

The flow in a turbine passage can be split into two regions, namely (i) a near wall region where the turbulent boundary layer has to be resolved, (ii) and the region further away from the blade surface where primarily the evolution of the free-stream turbulence has to be captured. This implies

a very fine grid requirement in the boundary layer, while the region farther away imposes a far less stringent grid requirement. To simulate this kind of flow, an overset grid approach is suitable, where the near wall region uses a O-type bodyfitting grid which is embedded in a periodic H-type grid in the passage. Such a capability has been implemented in the code written by Nagarajan et al (2003).

3.1 Discretization and time marching schemes

A sixth-order compact finite difference scheme of Lele (1992) is used to discretize the variables in space. A staggered arrangement of variables is employed, where the scalar variables are stored at the center of the grid cells while the velocity components are stored at their respective cell faces.

In order to optimise the cost of the computations, a mixed implicit-explicit time marching algorithm is used. The bodyfitting O-grid region is marched in time using a Beam-Warming type implicit scheme

$$\frac{3U^{n+1} - 4U^n + U^{n-1}}{2\Delta t} = -G(U^{n+1}, t^{n+1}) \quad (15)$$

where the solution at time levels n and $(n - 1)$ are used to find the solution at time level $(n + 1)$. In order to reduce the cost of the inversion, an approximate factorization of the right hand side G^{n+1} is applied. The background H-type mesh is marched using the standard RK-3 scheme. See Nagarajan (2004) for the details of the implementation.

3.2 Intergrid Communication

The solutions in the two grid zones are coupled through an overlap zone, where the data is interpolated between the grids using the fourth order Hermite interpolation scheme developed by Delfs (2001). In two dimensions, the Hermite interpolation at an overlap point is constructed using the function values and the first derivatives at the four surrounding points which bound the interpolated point in the uniform computational space. A local grid system (ξ, η) is constructed in the computational space, with the origin of the coordinate system at the center of the box formed

by the points bounding the interpolated point. The coordinates of the interpolated point in this coordinate system are found by the inverse mapping $(\xi, \eta) = M^{-1}(x, y)$. The forward mapping $M(\xi, \eta)$ is defined at all points using the Hermite interpolation scheme, and the inverse mapping $M^{-1}(x, y)$ is found using a Newton-Raphson procedure. The interpolation formula is give by

$$f(\xi, \eta) = \sum_{l,k=0}^1 C_{lk}^0(\xi, \eta) f_{i+l,j+k} + C_{lk}^\xi(\xi, \eta) \left[\frac{\partial f}{\partial \xi} \right]_{i+l,j+k} + C_{lk}^\eta(\xi, \eta) \left[\frac{\partial f}{\partial \eta} \right]_{i+l,j+k} + O(\Delta^4) \quad (16)$$

where C_{lk}^0 , C_{lk}^ξ , and C_{lk}^η are coefficients of interpolation. The details of the implementation can be found in Delfs (2001). Whereas Delfs uses the Dispersion Relation Preserving (DRP) finite difference scheme for computing derivatives, we use the sixth order compact finite difference scheme.

4 Summary of LES Code development

A high-order parallel compressible LES code developed by A. Xiong (2003) was used to study leading edge heat transfer. Another high-order parallel compressible LES capability to simulate transitory flows was developed under DoD ASC support by S. Nagarajan, based on the algorithm by Nagarajan, Lele and Ferziger (2003). Nagarajan et al (2007) used this solver to study the problem of bypass transition on model geometries with focus on the effects of leading-edge bluntness. It was possible to adapt any of these codes to do the full three-dimensional turbomachinery passage simulations. Nagarajan's code was chosen for the robustness and efficiency of his algorithm and its implementation.

Under this grant, Nagarajan's LES code was extended to study the flow and heat transfer in full turbine cascade passages. As a first step, iso-thermal wall boundary condition was implemented to study heat transfer. The conflicting requirements of maintaining turbulence resolution in the free-stream, capturing the vortex dynamics of turbulence as it is distorted in the turbine passage and especially around the leading-edge region, maintaining sufficient resolution in the viscous boundary layers, and allowing the substantial flow turning representative of turbine cascades required the development of a overset LES capability.

A computational issue in the simulation of HP turbine flows is the treatment of moving shocks which may arise in these transonic flow fields. Recently, Fiorina & Lele (2007) have developed a high-order nonlinear hyper-viscosity/hyper-diffusivity based shock capturing scheme for LES of supersonic combustion flows, such as a jet in supersonic cross-flow in SCRAM jet applications. These flows involve complex three-dimensional shock waves and its interaction with turbulence. We intend to implement this shock-capturing methodology in the overset LES code in the near future.

The overset mesh algorithm is designed to run efficiently on parallel computers and for this purpose special parallel solvers for large-banded matrices were implemented.

5 Results

The effect of free-stream turbulence on stagnation point flow and heat transfer was studied using the LES capability developed by Xiong (2003). It was observed that in the presence of free-stream turbulence, intense, quasi-streamwise vortices develop near the leading edge region, which were responsible for heat transfer augmentation. The results from this study are currently under review for publication in JFM. The manuscript has been included as an appendix to this report.

The new overset LES code is being used for the turbine passage simulation. This overset LES capability has been tested on 2D and 3D cases. The DNS of flow past a circular cylinder at $Re = 150$ and $Ma = 0.2$ was simulated on a 2D mesh. A body-fitted O-type grid of size 225×170 and a background H-type grid of size 670×500 was used. Figure 1 shows the dipole nature of the sound radiated by the cylinder. Figure 2 shows the excellent comparison with the pressure, lift and drag coefficients obtained from this simulation and the 2D DNS by Inoue and Hatakeyama (2002). A typical two dimensional simulation with half a million grid points took about 12 hrs on 8 Intel Xeon processors in order to get converged results.

Exploratory 2D and 3D simulations using the C3X HP vane geometry were performed. Figures 3-4

show results from a 2D DNS of the C3X HP cascade. A combination of O-type grid of size 400×45 around the blade and a background H-type grid of size 400×175 in the passage was used. The inlet Reynolds number based on the inlet velocity and chord of the blade was 50,000 and the inlet Mach number was 0.15. The simulation was initialized by the solution from a RANS computation of the passage using an in-house RANS code.

A preliminary 3D LES calculation was performed using the same grid as the 2D calculation, but with the 2D planar grid stacked in the spanwise direction to form a 3D grid. 32 spanwise points were used over a spanwise length of 30% chord. The solution from the 2D calculation was used to initialize the 3D calculation. Although no free stream turbulence was imposed, the wake from the blade was however observed to become turbulent. A way to quantify aerodynamic losses in the passage is to compute the wake loss coefficient along a line in the wake. The wake loss coefficient is defined as

$$\Omega = \frac{P_{t,in} - P_{t,ex}}{P_{t,in} - P_{s,ex}} \quad (17)$$

The wake loss profile for the 3D LES of the C3X cascade is shown in figure 5. The values seem to compare well with the experiments of Ames(1994), although the Reynolds number of the calculation was much lower and there was no external free stream turbulence.

These exploratory calculations have allowed us to gain confidence with the new Overset LES code. Simulations matching experimental conditions and with imposed external free-stream and wake turbulence will be conducted in the near future.

6 Summary

A thorough investigation of leading edge heat transfer has been performed using LES, with support from the current and a previous AFOSR grant. The results from the leading edge study have been presented at conferences and have also appeared as articles in archival journals (see references section). The focus has then shifted towards solving the full three-dimensional problem of flow in a turbine passage, including the effects of free-stream turbulence from the combustor, and the

unsteady interactions between various blade rows in the form of moving wakes and shocks. A high-order overset LES code suitable for the study of turbomachinery passages has been developed. Some preliminary results have been obtained using this code, mostly as cases for code validation. The code is currently being used to investigate flow in turbine passages under realistic conditions, and detailed comparisons with available experiments will be made. This study is expected to continue under a future grant from AFOSR.

7 Personnel

Professor Sanjiva Lele is the principal investigator for this project. A former graduate student Dr. Andy Xiong completed his dissertation with supported from this and a previous AFOSR grant. Another graduate student Rathakrishnan Bhaskaran's dissertation research was being supported by this grant.

8 References

- Ames, F. E. (1994) Experimental study of vane heat transfer and aerodynamics at elevated levels of turbulence, *NASA contractor report 4633*.
- Aris, R. (1989) Vectors, tensors, and the basic equations of Fluid Mechanics, *Dover Publications, Inc.*
- Delfs, J. W. (2001) An overlapped grid technique for high resolution CAA schemes for complex geometries. AIAA Paper 2001-2199.
- Fiorina B. and S.K. Lele (2007) An artificial nonlinear diffusivity method for supersonic reactive flows with shocks, *J. Computational Physics*, v. 222, p. 246-264.
- Inoue, O. and N. Hatakeyama (2002) Sound generation by a two-dimensional circular cylinder in a uniform flow. *J. of Fluid Mechanics*, v. 471, p. 285-314.

- Lele, S.K. (1992) Compact finite difference schemes with spectral-like resolution, *J. of computational physics*, v. 103, p. 16-42.
- Nagarajan S., S.K. Lele, and J.H. Ferziger (2007) Leading edge effects in bypass transition, *J. Fluid Mech.*, v.. 572, p. 471-504.
- Nagarajan S., S.K. Lele, and J.H. Ferziger (2003) A robust high-order compact method for large eddy simulation, *J. Computational Physics*, v. 191, p. 392-419.
- Nagarajan S. (2004) Leading edge effect in bypass transition, *PhD Thesis*, Stanford University.
- Xiong Z. and Lele, S. K. (2003) Simulation and analysis of stagnation point heat transfer under free-stream turbulence, AIAA paper 2003-1259.
- Xiong Z. and Lele, S. K. (2004) Distortion of upstream disturbances in Hiemenz boundary layer, *J. Fluid Mech.*, v. 519, p. 201-232.

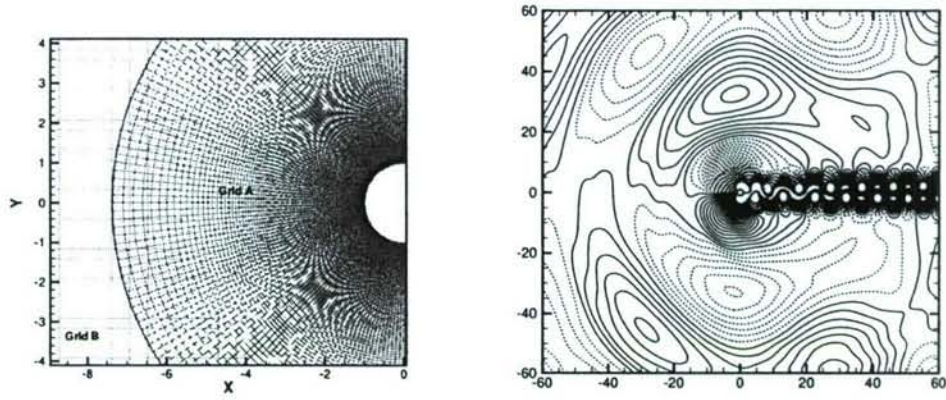


Figure 1: (a) The grid used for the cylinder simulation, showing the overlap region between the O- and H-type grids. (b) Fluctuation pressure field ΔP , showing the dipolar nature of sound field radiated by the cylinder. The contour levels are from $\Delta P_{min} = -0.1M^{2.5}$ to $\Delta P_{max} = 0.1M^{2.5}$ with an increment of $0.0025M^{2.5}$. solid line, $\Delta P > 0$; \cdots , $\Delta P < 0$.

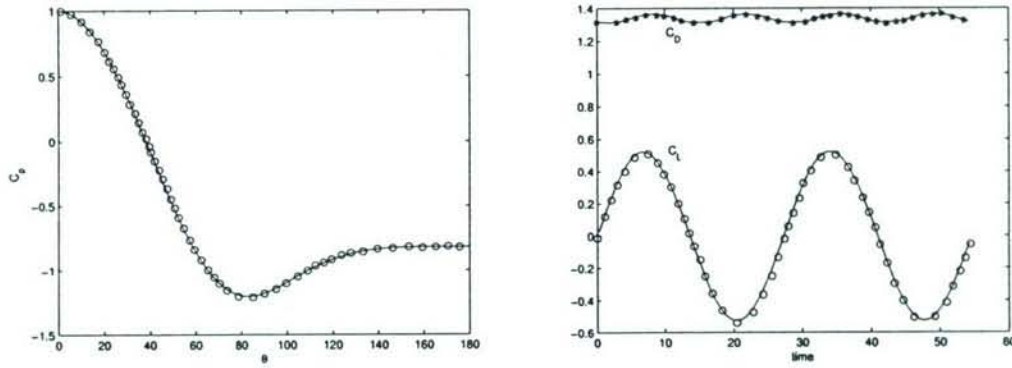


Figure 2: Cylinder simulation: (a) Time averaged pressure coefficient. (b) Time history of lift and drag coefficients. Lines: Current simulation, Symbols: Simulation by Inoue and Hatakeyama (2002).

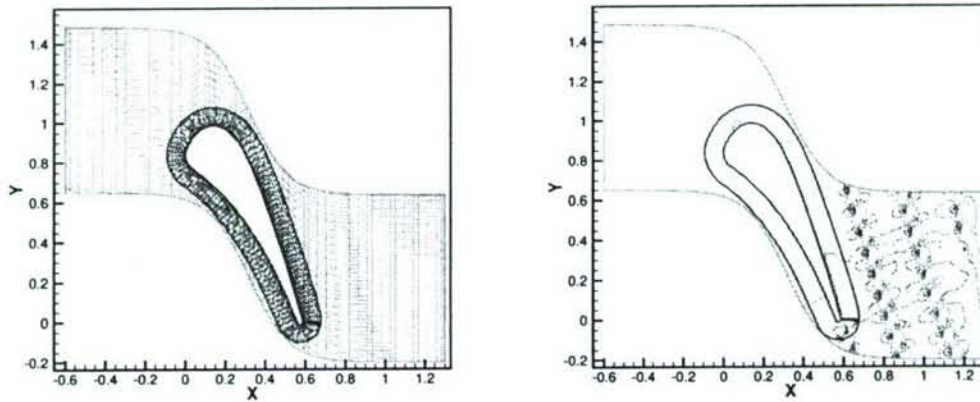


Figure 3: 2D C3X HP cascade simulation: (a) The grid used for the C3X HP cascade simulation, showing the overlap region between the O- and H-type grids. Every fourth grid point has been shown. (b) ρv contours showing the wake shed by the blade.

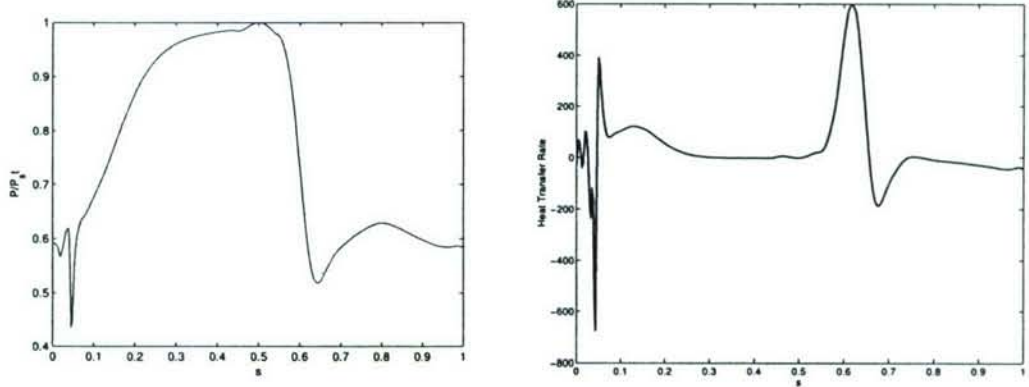


Figure 4: 2D C3X HP cascade simulation: (a) Pressure and (b) heat transfer to the blade.

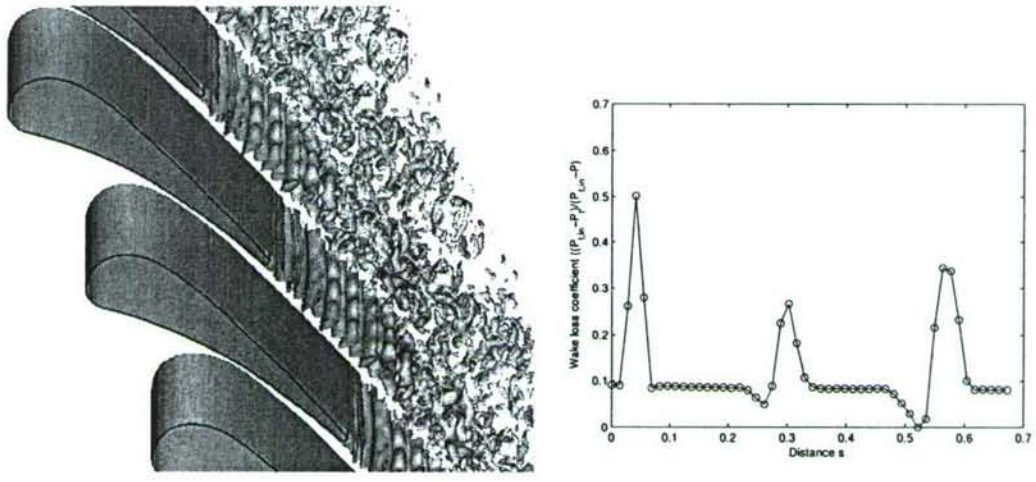


Figure 5: 3D C3X HP cascade simulation: (a) Iso-surfaces of spanwise vorticity show the turbulent nature of the wake. (b) Wake loss coefficient along a line in the wake perpendicular to the blade chord.

Stagnation Point Flow Under Free-Stream Turbulence

By ZHONGMIN XIONG[‡] AND SANJIVA K. LELE

Department of Mechanical Engineering, Stanford University, Stanford, CA 94305, USA

(Received ?? and in revised form ??)

In this paper, the effects of free-stream turbulence on stagnation point flow and heat transfer are investigated through Large Eddy Simulation (LES) of homogeneous isotropic turbulence impinging upon an isothermal elliptical leading edge. Turbulent mean flow and Reynolds stress profiles along the stagnation streamline, where the mean flow is strain dominant, and at different downstream locations, where the mean flow gradually becomes shear-dominated, are used to characterize evolution of the free-stream turbulence. The Reynolds stress budgets are also obtained, and the turbulence anisotropy is analyzed through the balance between the mean flow strain and the velocity pressure gradient correlation. In the presence of free-stream turbulence, intense, quasi-streamwise vortices develop near the leading edge with a typical diameter on the order of the local boundary layer thickness. These strong vortices cause the thermal fluxes to peak at a location much closer to the wall than that of the Reynolds stresses, resulting a greater sensitivity to free-stream turbulence for the heat transfer than the momentum transfer. The heat transfer enhancement obtained by the present LES agrees quantitatively with available experimental measurements. The present LES results are also used to examine the eddy viscosity and pressure strain correlations in Reynolds stress turbulence models.

[‡] Current address: Lawrence Livermore National Laboratory, Livermore, CA, 94550, USA

1. Introduction

Stagnation point flow, where fluid approaching a solid surface divides into diverging streams, occurs ubiquitously in nature as well as in many engineering problems. An improved understanding of the stagnating flow turbulence and heat transfer is critical to a wide range of engineering applications, from protecting a gas turbine blade from being melted by the extremely hot and turbulent combustion gas, to enhancing the efficiency of modern micro-electronics cooling system using micro-jet array impingement.

In his pioneering work, Hiemenz established that stagnation point flow is one of the very few types that admit exact solutions of Navier-Stokes equations. Subsequent studies have been focused on understanding perturbed stagnation point flows, i.e. the evolution and effects of various disturbances, including turbulence, that are present in the free stream. One of the prominent effects, first observed in 1920s (Piercy & Richardson 1928, 1930), is that free-stream turbulence induces large heat transfer enhancement at the stagnation point (Giedt 1949; Hegge-Zijnen 1957; Kestin *et al.* 1961). Various semi-empirical correlations have been proposed to quantify this effect, mostly based on the mean flow Reynolds number and the free-stream turbulence intensity (Smith & Kuethe 1966; Kestin & Wood 1971; Lowery & Vachon 1975; Mehendale *et al.* 1991), but they are met with limited success. Later, turbulence length scale was recognized to play a critical role in determining the overall effects of free-stream turbulence. By incorporating turbulence length scale into the correlations, the applicability of prediction correlation is significantly improved (Ames & Moffat 1990; Van Fossen *et al.* 1995; Dullenkopf & Mayle 1995). Although different definitions of length scale are used in these correlations, the heat transfer enhancement is found generally to increase with increasing Reynolds number and turbulence intensity, but decrease with increasing turbulence length scale.

Theoretical studies of the free-stream turbulence effects in stagnation point flows have

ranged from the mean flow unsteadiness, the linear/nonlinear instability, to the vortex stretching/amplification effects. Lighthill (1954) studied a pulsating mean flow around a cylindrical body and obtained the Stokes-layer correction, but no significant change in heat transfer was found. Similarly modulated stagnation point flows were also studied by Ishigaki (1970), Pedley (1972) and Merchant & Davis (1989), but with an emphasis on the skin friction. The linear stability analysis was initiated by Görtler (1955) and Hämmerlin (1955), further extended by Kestin & Wood (1970), and finally clarified by Wilson & Gladwell (1978). It has shown that plane stagnation point flow is always linearly stable to three dimensional disturbances. For finite amplitude disturbances, Lyell & Huerre (1985) showed that the flow can be destabilized if the level of the external two- or three dimensional disturbances exceeds a threshold value. Recently, the linear instability for the more general attachment-line boundary layer flow has also been investigated by Lin & Malik (1996) and Theofilis *et al.* (2003). Morkovin (1979) argued that the enhancement of heat transfer is more likely a result of forced response to upstream disturbances as opposed to any internal flow instability, a view advocated earlier by Suter (1965) who analyzed the amplification of incoming organized disturbances by mean strain, indicating the sensitivity of the heat transfer to vortical disturbances. For turbulence impinging on a circular cylinder with either very large or very small scales, Hunt (1973) obtained the behavior of second order turbulence statistics by using a generalized rapid distortion theory (RDT). Xiong & Lele (2004) showed the critical parameter in determining the evolution of upstream three-dimensional disturbance is the ratio between the disturbance length scale to the Hiemenz boundary layer thickness. Using numerical simulation of a swept Hiemenz boundary layer, Spalart (1989) found that, out of initial white-noise disturbances, the most unstable disturbance-mode is the one with the same similarity form as the mean Hiemenz flow, an assumption made in the stability analysis mentioned

above. The flow structures induced by free-stream turbulence in a stagnation region were found to be qualitatively similar to those induced by upstream organized disturbances (Xiong & Lele 2001). Bae *et al.* (2000) showed that different length scales generate quite different flow patterns and in turn different heat transfer responses in a plane stagnation point flow. Although much progress has been made over the years, a complete understanding of the effects of free-stream disturbances, particularly turbulence, in stagnation point flows has not been achieved.

The free-stream turbulence effects have also proven difficult to be incorporated in engineering turbulence models. The one equation model, e.g. Spalart & Allmaras (1992), while widely used and shown to be particularly successful in aerodynamic flows (Bardina *et al.* 1997; Wilcox 2001), does not explicitly account for the effects of free-stream turbulence. Standard two equation models, e.g. $k - \epsilon$ or $k - \omega$ model, when used in stagnation point turbulent flows, badly over predict the turbulent kinetic energy and heat transfer — this is termed as “stagnation point anomaly” (Durbin 1996; Champion & Libby 1994, 1991). A fundamental difficulty with the two equation models is that turbulence is assumed to be predominately isotropic and in quasi-equilibrium. But stagnating flow turbulence can be strongly anisotropic because different components of the fluctuation velocity respond differently to the mean flow straining. Reynolds stress models provide the generality to account for the anisotropy of the turbulence explicitly. Im *et al.* (2002) used three variants of Reynolds stress model, the GL model (Gibson & Launder 1978), the GL-CL model (Craft *et al.* 1993) and the SSG model (Speziale *et al.* 1991), to compute both the impinging and counter-current stagnation flows. Although the predictions from these models were better than $k - \epsilon$ type models, all the models still severely over-predict the turbulence kinetic energy, and have large discrepancies in other Reynolds stress components when compared to experimental measurements. The problem stems

from the over prediction of the energy production and the under prediction of the redistribution by the pressure strain correlations. This uncertainty may be attributed to the difficulty in, and hence the lack of, detailed experimental measurements in the immediate vicinity of the leading edge.

In this study, we carry out LES of the impingement of free-stream turbulence upon an isothermal elliptical leading edge. To allow direct comparison with experimental results, the flow configuration and simulation parameters are taken to match the experiments by Van Fossen *et al.* (1995). The first goal of the present study is to gain an improved understanding on the evolution of stagnating flow turbulence and the mechanism of the heat transfer enhancement. Secondly, the simulation is aimed to help reduce some of the uncertainty in turbulence modelling for strain-dominated flows. The relative magnitudes and distributions of various turbulence quantities are obtained from the LES data. The present simulation shows that the largest change in the turbulence structure occurs in the immediate region of the leading edge. Thirdly, it is hoped the present LES data may help the general development and calibration of turbulence models when turbulence anisotropy becomes strong.

The rest of the paper is organized as follows. The basic governing equations for the LES are given in section 2. The numerical methods and validation procedures are described in section 3, along with a blending scheme for generating free-stream turbulence. The main simulation results, including the mean flow profiles, turbulence intensity and Reynolds stress budget, are presented in section 4. In section 5, we summarize the results and give concluding remarks.

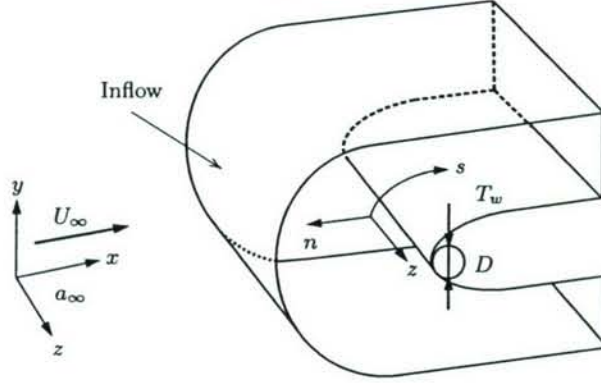


FIGURE 1. Flow configuration and inflow, outflow and wall boundary

2. Navier-Stokes equation and SGS modeling

The flow configuration for the present LES is shown in figure 1 with both the laboratory coordinates (x, y, z) and the local surface coordinate (s, n, z) labelled. The mean flow is two-dimensional and the turbulence is assumed to be homogeneous in spanwise direction z .

The governing equations for the LES of compressible turbulence are the filtered Navier-Stokes equations. With the dynamic subgrid stress (SGS) model for compressible flows (Moin *et al.* 1991), they are written as

$$\bar{\rho}_{,t} + (\bar{\rho}\bar{u}_i)_{,i} = 0 \quad (2.1)$$

$$\bar{\rho}\bar{u}_{i,t} + \bar{\rho}\bar{u}_j\bar{u}_{i,j} = -\bar{p}_{,i} + \frac{1}{Re} [(\bar{\lambda}\bar{u}_{j,j})_{,i} + (2\bar{\mu}_T\bar{S}_{ij})_{,j}] \quad (2.2)$$

$$\begin{aligned} \bar{\rho}\bar{T}_{,t} + \bar{\rho}\bar{u}_i\bar{T}_{,i} + (\gamma - 1)\bar{\rho}\bar{T}\bar{u}_{j,j} &= \frac{\gamma}{PrRe} [\bar{\kappa}_T\bar{T}_{,i}]_{,i} + \\ &\frac{\gamma(\gamma - 1)M^2}{Re} [\bar{\lambda}\bar{S}_{ii}\bar{S}_{jj} + 2\bar{\mu}\bar{S}_{ij}\bar{S}_{ij}], \end{aligned} \quad (2.3)$$

where

$$\bar{p} = \frac{\bar{\rho}\bar{T}}{\gamma M^2} + \frac{2}{3}C_I\bar{\rho}\Delta^2|\bar{S}|^2 \quad (2.4)$$

$$\bar{\mu}_T = \bar{\mu} + C\bar{\rho}\Delta^2|\bar{S}|Re \quad (2.5)$$

$$\tilde{\kappa}_T = \tilde{\kappa} + C\bar{\rho}\Delta^2|\tilde{S}|\frac{PrRe}{\gamma Pr_t}. \quad (2.6)$$

Here the tilde stands for Favre average; ρ is the density; u_i is the velocity vector, and T is the temperature. μ_T is the subgrid eddy viscosity. κ_T is the subgrid eddy thermal conductivity, and Pr_t is the turbulent Prandtl number. $S_{ij} = \frac{1}{2}(u_{i,j} + u_{j,i})$ is the rate-of-strain tensor. M , Re are the mean flow Mach number and Reynolds number, and in the present study they are based on the upstream mean velocity U_∞ , the speed of sound a_∞ and the leading edge diameter D . $Pr = 0.7$ is molecular Prandtl number and $\gamma = 1.4$ is the ratio of specific heats. The eddy coefficients C_I for the subgrid normal stress is set to zero and the turbulence Prandtl number Pr_t is set to unity. The eddy coefficient C for the subgrid shear stress is computed using the standard dynamic SGS model, see (Xiong 2004) for details.

3. Numerical Method

The numerical method and validation problems for the present LES are described briefly in this section. For more details, the reader is referred to Xiong (2004).

3.1. Implicit scheme with linearized subiterations

We first recast the compressible flow governing equations in a general form:

$$U_{,t} + F(U) = 0 \quad (3.1)$$

where $U = \{\rho, u, v, w, T\}^T$ is the vector of flow variables and $F(U)$ represents the nonlinear and viscous terms. Since for wall-bounded flows, explicit time integration schemes are prohibitively expensive because of the CFL stability constraint, in this study we use an implicit dual-time stepping scheme with linearized subiteration, which may be expressed as

$$\left[I + \frac{3\Delta\tau}{2\Delta t} I + \Delta\tau A(U^n) \right] \Delta U^k = -\Delta\tau \mathcal{R}^k \quad (3.2)$$

with

$$\mathcal{A} \equiv \frac{\partial F}{\partial U}, \quad \mathcal{R}^k = \frac{3U^k - 4U^n + U^{n-1}}{2\Delta t} + F(U^k), \quad \Delta U^k = U^{k+1} - U^k. \quad (3.3)$$

Here Δt is the physical time step, and $\Delta \tau$ is the pseudo time step for subiteration. At each physical time step, U^n is taken to be the initial value for U^k to start the subiteration at $k = 0$. If the subiteration converges, i.e. $\Delta U^k \rightarrow 0$ one gets $U^{k+1} = U^k$. The final value of U^{k+1} is taken to be U^{n+1} , and $\mathcal{R}^{n+1} = 0$ recovers the second order fully implicit scheme, which is unconditionally stable. Notice that instead of a function of U^k as in standard subiteration schemes, the left hand side operator in (3.2) is only a function of U^n ; therefore (3.2) is linear for variable ΔU^k . A LU decomposition of the coefficient matrices is performed at the first step of each subiteration, and the factored matrices are stored and used until the subiteration converges. This obviates the need for inverting the coefficient matrices at every subiteration step, and therefore significantly improves the subiteration efficiency.

3.2. Spatial Discretization

At interior nodes, the five-point central difference scheme is used for first and second derivatives. Near the computational boundaries, five-point biased stencils are used. The resulting difference schemes are fourth and third order accurate for the first and second derivatives, respectively. Owing to the intrinsic non-dissipative nature, central difference schemes are often subject to the so-called two- δ wave instability caused by the decoupling of the even and odd grid points. In the LES context, one should not expect that a physics-based SGS model will automatically suppress such an instability. Beside the fact that the SGS model itself is often implemented with the same central difference scheme, the length scale of the two- δ waves is much shorter than that of the SGS model. The purpose of the SGS model is to extract energy at a correct rate at a cutoff scale—the scale at

which the discrete representation becomes inadequate— and, for a grid spacing h , this is typically around a wavenumber of $hk \sim \pi/2$. But for the two- δ wave, it occurs at the Nyquist wavenumber $hk \sim \pi$. Hence to suppress the two- δ waves, appropriate numerical damping procedures must be applied. In the present simulations, we choose the following fourth-order dissipation

$$D_n = -\epsilon_d \left(\Delta_\xi^4 \frac{\partial^4 U}{\partial \xi^4} + \Delta_\eta^4 \frac{\partial^4 U}{\partial \eta^4} + \Delta_z^4 \frac{\partial^4 U}{\partial z^4} \right) \quad (3.4)$$

where ϵ_d is the amplitude of the dissipation, and Δ_ξ , Δ_η and Δ_z are the grid spacing in streamwise, normal and spanwise directions in computational space. Care must be taken to ensure that the added numerical dissipation is minimal and does not deteriorate the resolved solution. For this purpose, ϵ_d is chosen to be such that the magnitude of D_n is significantly smaller than the truncation error of the difference schemes. Based on modified wave number analysis, this may be achieved by requiring $\epsilon_d \leq 0.01N_g$, where $N_g = (N_\xi + N_\eta + N_z)/3$ is the average number of grid points in one spatial direction. The resulted D_n is one order of magnitude lower than the truncation error and its effects on the results of the present LES is expected to be negligible. A more detailed discussion of the method and the demonstration of its effectiveness can be found in Xiong (2004).

3.3. Boundary Conditions

Boundary conditions are introduced to replace the governing equations at the inflow, outflow and the wall boundaries of the computational domain. Consider an arbitrary boundary constraint at time level $n + 1$ on the flow variable $U = \{\rho, u, v, w, T\}$

$$\mathcal{B}(U^{n+1}) = 0. \quad (3.5)$$

The general implicit treatment of the boundary conditions, in terms of the variable $\delta U = U^{n+1} - U^n$, can be written as

$$\left(\frac{\partial \mathcal{B}}{\partial U}\right)^n \delta U = -\mathcal{B}(U^n) \quad (3.6)$$

The boundary condition at the inflow provides the upstream mean flow information and also introduces free-stream disturbances or turbulence into the computational domain. For a subsonic inflow, characteristic analysis shows that four incoming quantities must be specified along with one outgoing quantity computed from the interior domain. The specific choice of these quantities depends on the formulation of the problem. In this study, we constrain the entropy, spanwise and tangential velocities, and the incoming Riemann invariant. The outgoing Riemann invariant is computed by first order extrapolation from the interior points close to the boundary.

At the outflow, the parabolized Navier-Stokes equations is used following Collis (1997), i.e. the streamwise second order derivatives in the equations are neglected. In addition, the pressure gradient at the outflow is obtained from the corresponding potential flow solution. This treatment has shown to yield an adequate and stable outflow boundary conditions both for the laminar and turbulent flow computations. No slip and isothermal conditions are applied at the wall for the velocities and temperature, and periodicity condition is imposed in spanwise direction.

Prior to turbulence simulations, the code is first validated on problems of laminar compressible boundary layer at a leading edge. The velocity and temperature profiles are compared with analytic self-similar solutions. An leading edge acoustic receptivity problem is also computed and compared with previous numerical studies. These validation results are summarized in Appendix A.

3.4. Generation of free-stream turbulence

In this section, we describe a blending procedure combining independent but statistically equivalent realizations of homogeneous isotropic turbulence into a unified turbulent flow field which serves as a realistic representation of free-stream turbulence. Consider two such turbulence fields, $U^{(1)}$ and $U^{(2)}$, that need to be concatenated in x direction, we introduce a blending zone, extending from the interface into each of the fields by a short distance, and a linear combination

$$\mathbf{u} = \cos \theta \mathbf{u}^{(1)} + \sin \theta \mathbf{u}^{(2)}, \quad (3.7)$$

where θ varies smoothly from 0 to $\pi/2$ across the blending zone. The new field varies smoothly from one field to another and retains the mean values and second order statistics of the original fields. The dependence of θ on x within the blending zone introduces an extra dilatation field, but it can be removed by using the Helmholtz decomposition theorem for the velocity vector. In figure 2, we plot the energy spectra of two original and the blended turbulence fields. It can be seen that the energy spectrum of the blended field remains essentially the same as the originals. A very small amount of energy is present at the lowest wave number due to the increased length in the x -direction. More comparisons of energy spectra, as well as other quantities of interest, can be found in Xiong *et al.* (2004).

In the present LES, twelve realizations of such independent but statistically identical homogeneous isotropic turbulence fields are pre-computed using LES with the same dynamic SGS model. To keep the same spanwise domain size as in the main LES, these simulations are carried out in a rectangular box of the size $1.6D$, $1.6D$ and $0.4D$ in x , y and z direction, respectively. A $128 \times 128 \times 32$ grid is chosen to ensure the isotropy of the resulting turbulence. The code is adapted from a DNS code (Lui 2003) which uses

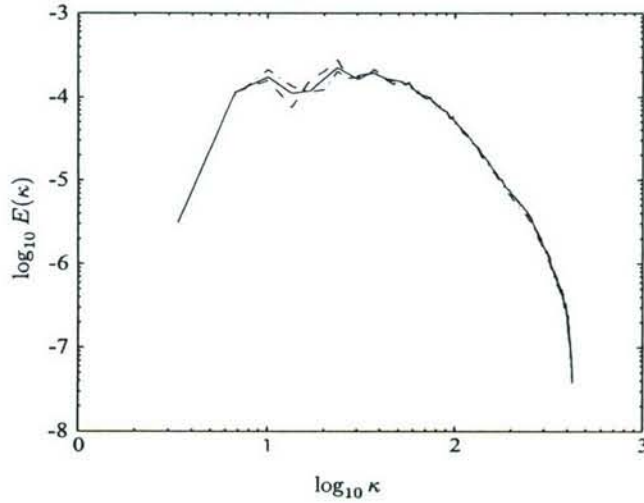


FIGURE 2. Energy spectra for the original and blended data sets. — · —: data 1,
 - - - - -: data 2, —: blended

a sixth-order compact finite differencing scheme and a fourth order Runge-Kutta time integration. Once the twelve turbulence fields are obtained, they are lined up spatially and joined together at the interfaces by applying the above blending procedure. The resulting turbulence field, twelve times longer than each individual realization but with the same characteristics, serves as the free-stream turbulence, which will be convected into the computational domain through the inflow boundary.

4. LES results

4.1. Simulation conditions

The flow condition for the present LES is taken from the wind tunnel experiments by Van Fossen *et al.* (1995), and specifically, corresponding to the data set No. 244. In the experiments, free-stream turbulence is generated by placing a turbulence-generating grid upstream of a leading edge model. The shape of the leading edge is a half-ellipse and the aspect ratio (length ratio between the major and minor axis) is 3 for this data set. Different values of turbulence intensity and length scale are obtained by varying the

Re_D	M_∞	Tu	L/D	Re_L	Re_T	T_w/T_0	domain (x, y, z)	$N_x \times N_y \times N_z$
42,000	0.15	0.05	0.1	210	93	1.075	(3.5D, 5D, 0.4D)	$191 \times 144 \times 48$

TABLE 1. Parameters of the mean flow and free-stream turbulence for the present LES.

mesh size of the grid and its location relative to the leading edge. The model is kept at a constant temperature, and the heat transfer rate is measured in the stagnation point region. The mean flow and free-stream turbulence parameters are summarized in Table 1. The mean flow Reynolds number $Re_D = U_\infty D/\nu$ is based on far upstream incoming velocity U_∞ and the leading edge diameter of curvature D . $M_\infty = U_\infty/a_\infty$ is the mean flow Mach number based on the sound speed a_∞ far upstream. Tu and L are the free-stream turbulence intensity and integral length scale; they are determined at the location of the leading edge but in the absence of the model. The numerical procedure for determining L from the auto-correlation measurements is given in Van Fossen *et al.* (1995) and applied in the present LES. $Re_L = TuL/\nu$ is the Reynolds number based on integral length scale and turbulence intensity and the Re_T is the Taylor microscale Reynolds number. T_w and T_0 are the surface temperature on the wall and the total or stagnation gas temperature in the free-stream.

The computational grid is generated by an algebraic multi-surface method (Eiseman 1985) in the $x - y$ plane which guarantees the grid orthogonality at the wall and the inflow/outflow boundaries. The grid points are clustered towards the wall and the stagnation point but uniformly spaced in spanwise direction. In the present LES study, a dual-grid approach is used. First, a large outer grid is generated covering half of the ellipse downstream and extending vertically from the bottom to the top wind tunnel wall.

A potential flow that matches the experimental base flow conditions is computed on this grid. For the subsequent LES calculations, a smaller inner grid covering only the leading edge region is extracted from the outer grid. On this inner grid, the the inflow/outflow boundary conditions for the mean flow can therefore be provided by the potential flow solution. This dual-grid approach enables us to improve the grid resolution near the leading edge at a reduced computational cost. For the LES grid, the minimum streamwise grid spacing is $\Delta x_{min}/D = 0.0037$ at the stagnation point, and the minimum normal spacing is $\Delta y_{min}/D = 0.00058$ at the wall. The Hiemenz scale for the laminar boundary layer, $\sqrt{\nu/A}/D = 0.0036$, is resolved by 7 grid points in the normal direction, here A is the outer flow strain rate. The time step for the present LES is $\Delta t = 0.0015$, and the total integration time $N\Delta t$ for obtaining the turbulence statistics is 25.

4.2. Mean flow results

The contour plots for the mean flow streamwise velocity U , transverse velocity V and temperature T are shown in figure 3. Outside the boundary layer, the difference between the mean and the laminar velocity contours are minimal, and along the stagnation streamline, the velocity profiles are almost indistinguishable (not shown here, see Xiong (2004)). It confirms the experimental measurements that the stagnation-line velocity is essentially independent of the free-stream turbulence. This is, however, not the case for the temperature profile. As shown in figure 4a, a steeper gradient is developed at the wall for the mean temperature profile (about 25 percent higher than the laminar value), indicating the heat transfer enhancement in the presence of free-stream turbulence.

The comparisons between the mean and laminar profiles of the tangential velocity U_s and the normalized temperature $(T - 1)/(T_w - 1)$ are further shown in figure 4b-d, using the local $s - n$ coordinates at three downstream locations $s/D = 0.2, 0.8$ and 1.6 (marked in figure 3c). The change of the slope at the wall is again about 25 percent for the

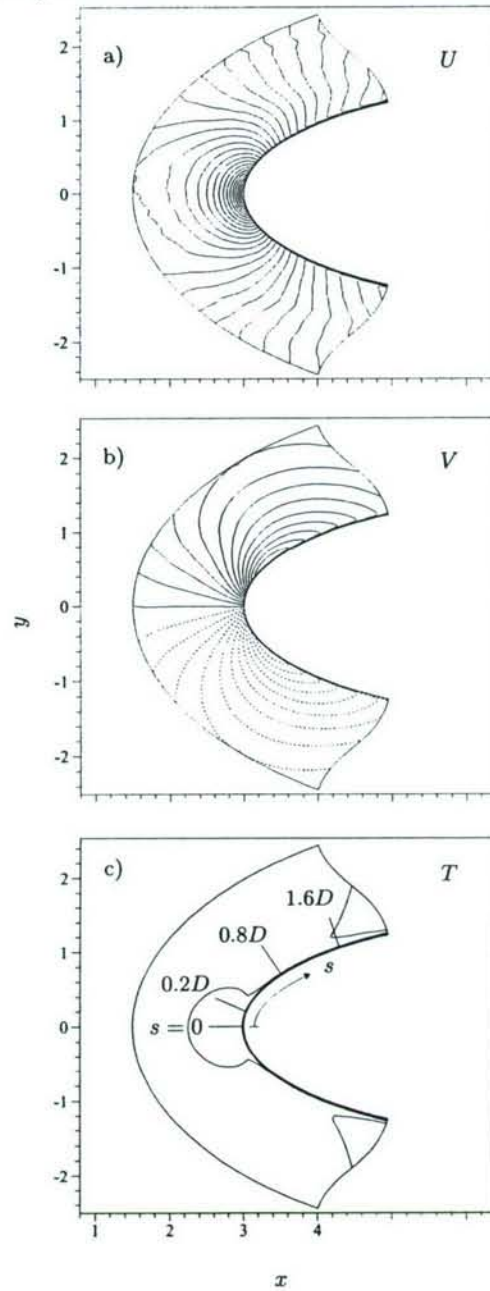


FIGURE 3. Turbulent mean velocity and temperature contours. $Re = 42,000$, $Ma = 0.15$, $Tu = 0.05$, $L/D = 0.1$. a) streamwise velocity U , contour minimum: 0.0 , maximum: 1.3, increment: 0.05. b) transverse velocity V , minimum: -0.6, maximum: 0.6, increment: 0.05. c) temperature T , minimum 0.995, maximum 1.075, increment:0.005. The streamwise locations of the four cross sections are also marked.

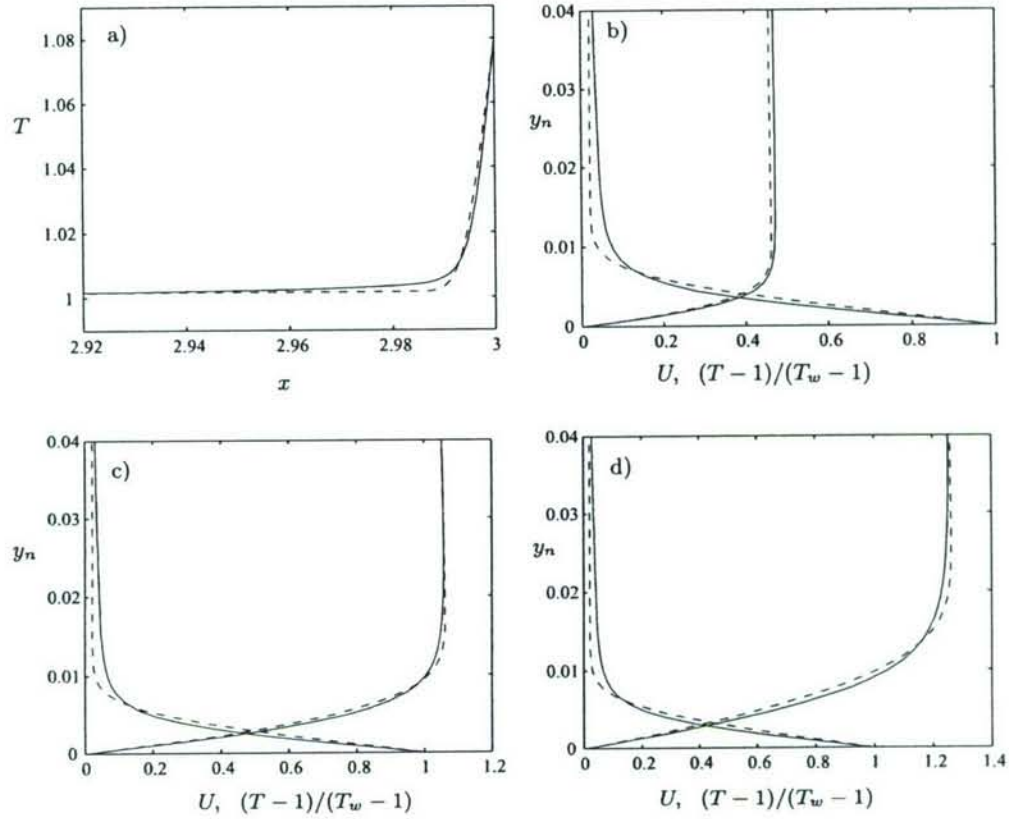


FIGURE 4. Comparison between turbulent mean and laminar velocity and temperature profiles at different streamwise locations, —: turbulent mean, - - - - -: laminar. $s/D = 0, 0.2, 0.8, 1.6$ from a) to d).

temperature and only about 5 percent for the velocity, signaling a greater sensitivity to the free-stream turbulence for the heat transfer than for the skin friction. Moreover, the profiles of the mean streamwise velocity also show that, despite the impinging turbulence, the boundary layer remains pre-transitional. A longer streamwise distance is needed than the present simulation domain before a fully turbulent boundary layer can develop.

4.3. Vortex dynamics

Figure 5 shows a visualization of instantaneous spanwise velocity within the $x - y$ plane at $z = 0$, and the temperature gradient on the model surface near the stagnation point

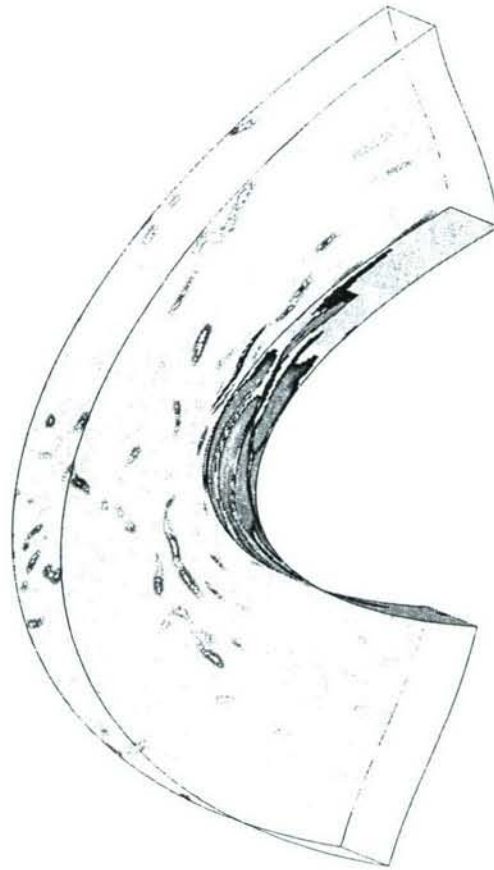


FIGURE 5. Instantaneous spanwise velocity in $x - y$ plane and temperature gradient on the body surface.

$s = 0$. It can be seen that the isotropic free-stream turbulent eddies have been strongly stretched in the streamwise direction near the stagnation point. The ensuing impingement of these vortices on the leading edge modifies the underlying thermal boundary layer dramatically. On the model surface, the resulting heat transfer distribution develops into thin, streamwise elongated streaky structures. The corresponding instantaneous temper-

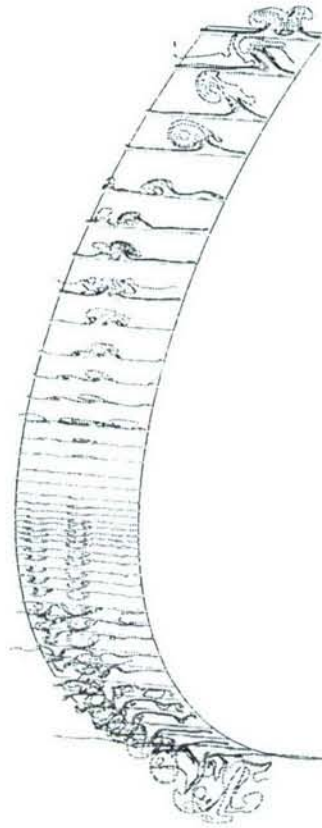


FIGURE 6. Instantaneous temperature contours at different locations on the body surface,
 $s/D = -0.8 \sim 0.8$.

ature fields are shown in figure 6 through a series of wall normal sections at different streamwise locations. The temperature contours show distinctive mushroom-like structures. By tracing these structures in consecutive sections, one easily sees the elongated streaky vortices being wrapped around the leading edge by the mean flow.

To better understand the typical vortex structures and their effects on heat transfer, the temperature contour and the corresponding velocity field in the stagnation plane $s = 0$ are shown in figure 7. The velocity fields show clearly that strong, amplified y -oriented vortices produce reverse flow ($u < 0$) in the stagnation region, which lifts up

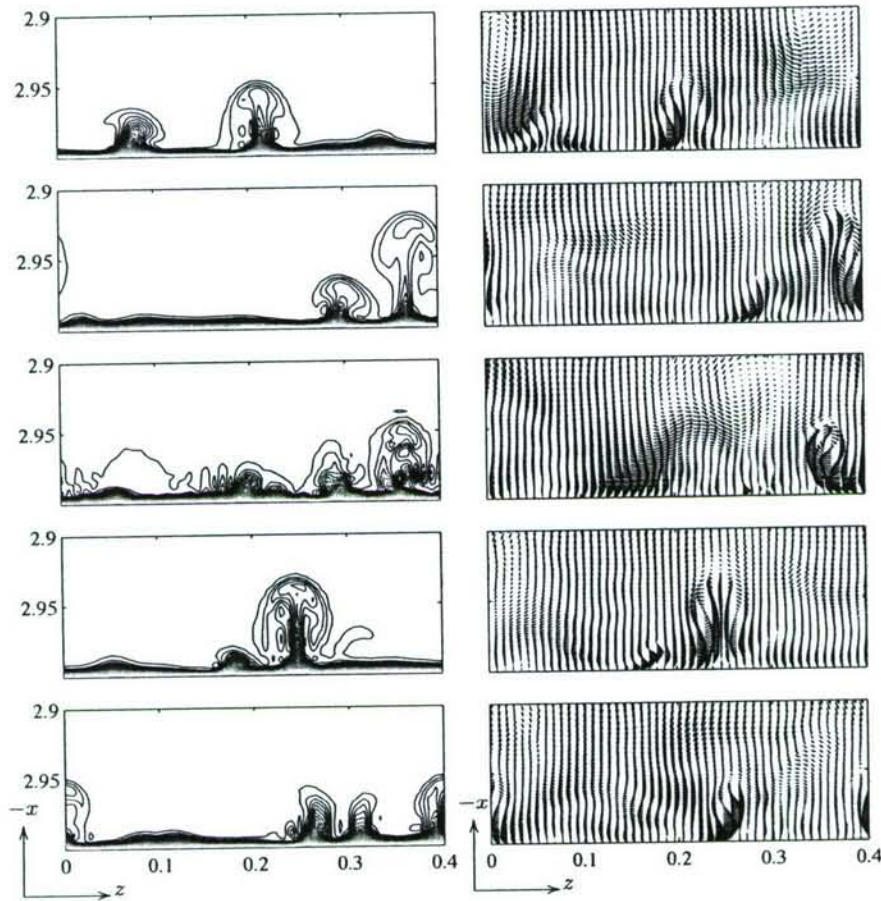


FIGURE 7. Temperature contour and the corresponding velocity field in the stagnation plane at different times. The mean flow direction is downward and the time interval is $\Delta t = 0.6$.

the hot fluid close to the wall and swaps it with the lower temperature fluid away from the wall. In doing so, the velocity disturbance creates the mushroom-like structures in the temperature contours. Directly underneath these mushroom-like structures, however, the thermal boundary layer is thicker than the undisturbed case — the heat transfer rate decreases. It is in the region between these mushroom-like structures, where the disturbed flow has a normal velocity directed towards the wall, that the boundary layer become thinner, and consequently the heat transfer increases. The overall spanwise averaged heat

transfer rate is thus determined by the distribution and intensity of these thickened and thinned regions.

As shown in figure 7, the mushroom-like structures typically do not remain at a fixed spanwise location; instead they move laterally over a significant distance during their lifetime. This indicates the lateral movement of the strong streamwise vortices by which these mushroom structures are formed. When a vortex approaches a wall, vorticity is generated at the wall through the no-slip boundary condition; therefore, the lateral movement of the vortices may be characterized through the movement of the wall vorticity. By following the slowest descent line on the space-time correlation, the average lateral speed for the wall vorticity along the stagnation line (z -axis) is found to be ± 0.06 , which is about half of the maximum w_{rms} at the leading edge. The mechanism of the lateral movement can be understood through the so-called wall-blocking effect. Considering a single vortex approaching a wall, an inviscid image vortex with opposite sign is induced at an equal distance on the other side of the wall to enforce the no-penetration wall boundary condition. The mutual induction of these two vortices generates a tangential velocity whose magnitude is proportional to the strength of the vortices. This causes the lateral movement of the approaching vortex in the spanwise direction, and in turn the movement of the mushroom structures in the temperature contours.

The stretching of the free-stream turbulence eddies may further be characterized quantitatively using spanwise two-point correlations of velocity. Figure 8 shows the streamwise velocity correlation at different locations along the stagnation streamline. At the inflow boundary, the correlation length is long, representing the length scale of the free-stream turbulence in the absence of the strain effect. Once the turbulence enters the domain, the spanwise length scale decreases monotonically and close to the leading edge it reaches a scale of local boundary layer thickness. A model problem on the competition between

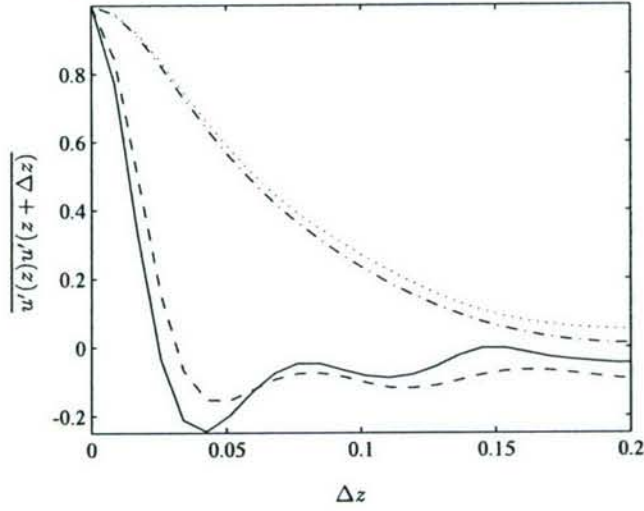


FIGURE 8. Two point correlation of streamwise velocity in spanwise direction along stagnation streamline. $\cdots\cdots$: $x = 1.55D$, $-\cdot-$: $x = 2.0D$, $-----$: $x = 2.97D$ (in the free stream), and $—$: $s = 2.99D$ (within the boundary layer).

the amplification due to vortex stretching and damping due to viscosity in a disturbed Hiemenz boundary layer was studied by Xiong & Lele (2004), and the leading edge region of the present flow represents the same process in the context of a complete flow field. We should also remark that because of this monotonic decrease of the turbulence spanwise length scale, the choice of the spanwise simulation domain size is a balance between encompassing the large scale free-stream turbulence at the inflow and sufficiently resolving the intense, small-scale streamwise vortices at the leading edge. In the present LES, we place our focus at the leading edge region and have chosen the spanwise domain size to be four times the integral length of the free-stream turbulence. A similar LES with spanwise domain size about seven times of the turbulence length scale was also performed in Xiong (2004). The comparison between the two cases suggests that the LES results are not sensitive to the spanwise domain size as long as the small scale vortices at the leading edge are adequately resolved.

The spanwise averaged non-dimensional heat transfer coefficient, denoted by Frössling

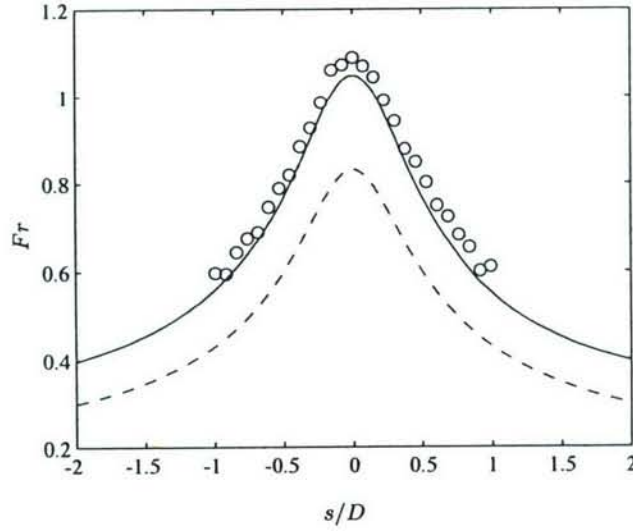


FIGURE 9. Averaged Frössling number distribution on the body surface. —: turbulent mean, - - - - -: laminar, \circ : experimental data (Van Fossen *et al.* 1995).

number $Fr = Nu/\sqrt{Re_D}$, where Nu being the Nusselt number, is plotted in figure 9 as a function of the streamwise distance from the stagnation point. The experimental measurements from Van Fossen *et al.* (1995) are also plotted for comparison. Both the LES and experimental results show that the shape of the Fr distribution is largely the same as in the laminar case, but their values are significantly higher in the presence of free-stream turbulence. Although the present LES result is slightly lower than the experimental measurements, as not all of the turbulence scales are resolved in LES, the overall agreement is good. As shown by Xiong & Lele (2004), there is an optimal length scale for the stagnation point heat transfer enhancement; scales larger or smaller than the optimum produce a smaller heat transfer enhancement. In order to accurately predict the free-stream turbulence effects, it is thus important to resolve the turbulence structures up to the optimal length scale. For this reason, the effect of SGS modelling needs to be evaluated. A typical distribution of the instantaneous SGS eddy viscosity ν_T is shown in figure 10a, and the corresponding time averaged distribution is shown in figure 10b.

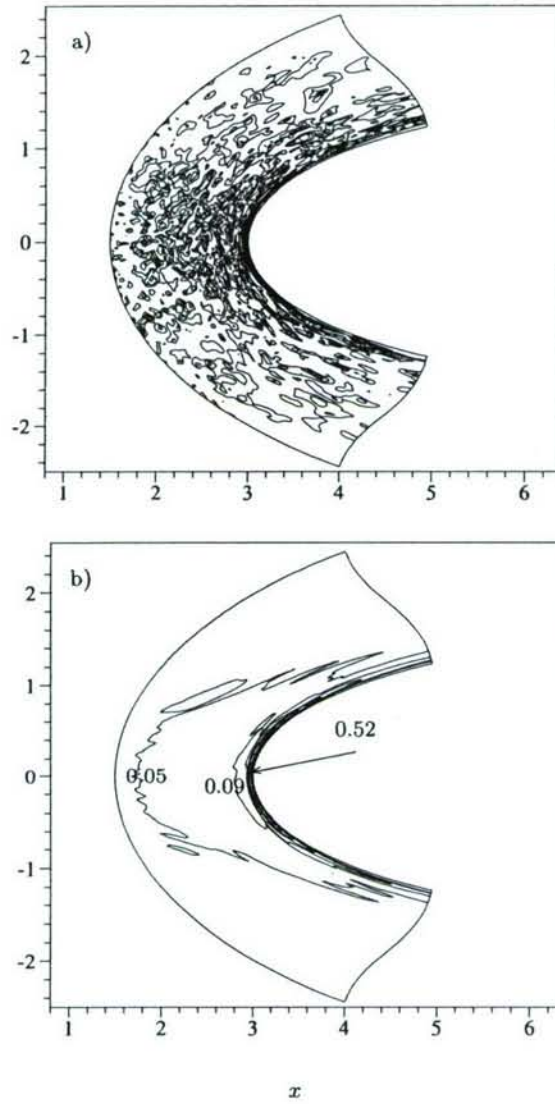


FIGURE 10. Contours of SGS eddy viscosity ν_T/ν . a) Instantaneous (averaged in z), contour minimum : 0.05, maximum: 0.75, increment: 0.014. b) Turbulent mean, minimum : 0.05, maximum: 0.52, increment: 0.040.

Both figures show that the maximum ν_T occurs in the leading edge region, where small scale turbulence is produced by strong vortex stretching and amplification. However, the value of ν_T is relatively small, about half of the molecular viscosity, indicating that

the grid resolution close to the wall is adequate for capturing the near wall eddies. In this sense, the present LES is essentially a quasi-DNS of the near wall flow. However, because of the grid stretching in the wall normal direction, outside the boundary layer the turbulence scales are not completely captured, and we have found the SGS eddy viscosity is necessary to prevent the solution from diverging caused by the intermittent passage of strongly stretched vortices outside the boundary layer.

4.4. Reynolds stress and turbulence budgets

Because of the spanwise homogeneity, the significant Reynolds stresses in the present flow are $\overline{u'^2}$, $\overline{v'^2}$, $\overline{w'^2}$, and $\overline{u'v'}$, and the significant heat fluxes are $\overline{u'T'}$, $\overline{v'T'}$. Along the stagnation streamline, the symmetry in y direction also leads to $\overline{u'v'} = \overline{v'T'} = 0$.

It is instructive to write the governing equations for Reynolds stress and heat transport. Using the notion of Reynolds average and letting \bar{f} denote the time averaged value of f , we may decompose the turbulence field into a mean and a fluctuation part, i.e.

$$\rho = \bar{\rho} + \rho', \quad u_i = U_i + u'_i, \quad p = P + p', \quad T = \bar{T} + T', \quad (4.1)$$

and similarly for the transport coefficients

$$\lambda = \bar{\lambda} + \lambda', \quad \mu_T = \bar{\mu} + \mu', \quad \kappa_T = \bar{\kappa} + \kappa'. \quad (4.2)$$

The steady transport equation for the Reynolds stress $\overline{u_i u_j}$ can be written as

$$\begin{aligned} \bar{\rho} U_k \overline{(u'_i u'_j)_{,k}} &= -\overline{u'_j p'_{,i}} - \overline{u'_i p'_{,j}} \\ &\quad - U_{i,k} [\bar{\rho} \overline{(u'_k u'_j)} + U_k \overline{\rho' u'_j} + \overline{\rho' u'_k u'_j}] \\ &\quad - U_{j,k} [\bar{\rho} \overline{(u'_k u'_i)} + U_k \overline{\rho' u'_i} + \overline{\rho' u'_k u'_i}] \\ &\quad - \bar{\rho} \overline{u'_k (u'_i u'_j)_{,k}} - \overline{\rho' u'_k (u'_i u'_j)_{,k}} \\ &\quad + \Phi_T \end{aligned} \quad (4.3)$$

On the right hand side of (4.3), the first row is the velocity pressure gradient correlation;

the second and the third rows are the production terms; the fourth row is the transport of Reynolds stress due to turbulent fluctuation. For incompressible flow, it can be reduced to a divergence form and is termed as turbulence transport. Here, for compressible flow, we use the term turbulence convection to refer to the sum of these two terms. The Φ_T in the last row is the total dissipation

$$\begin{aligned}
\Phi_T &= \frac{1}{Re} [(\bar{\lambda} \overline{D'_{,i} u'_j} + \overline{D_{,i} \lambda' u'_j} + \overline{\lambda' D'_{,i} u'_j}) + \\
&\quad (\bar{\lambda} \overline{D'_{,j} u'_i} + \overline{D_{,j} \lambda' u'_i} + \overline{\lambda' D'_{,j} u'_i})] \\
&+ \frac{2}{Re} [(\bar{\mu} \overline{S'_{ik,k} u'_j} + \overline{S_{ik,k} \mu' u'_j} + \overline{\mu' S'_{ik,k} u'_j}) + \\
&\quad (\bar{\mu} \overline{S'_{jk,k} u'_i} + \overline{S_{jk,k} \mu' u'_i} + \overline{\mu' S'_{jk,k} u'_i})] \\
&= \varepsilon + \Phi_v
\end{aligned} \tag{4.4}$$

where $D \equiv u_{i,i}$ is the divergence of the velocity field; ε is the turbulence dissipation rate defined by

$$\varepsilon = \frac{2}{Re} \overline{\mu u'_{i,k} u'_{j,k}} \tag{4.5}$$

and the remaining term $\Phi_v = \Phi_T - \varepsilon$ is loosely termed as viscous diffusion by analogy to the incompressible flow case, although it also contains terms involving dilatation and fluctuation in the turbulent viscosity coefficient.

Similarly, for turbulence heat flux $\overline{u'_i T'}$, we may also write

$$\begin{aligned}
\overline{\rho U_k (u'_i T')_{,k}} &= -\overline{T' p'_{,i}} \\
&- \overline{T}_{,k} [\overline{\rho u'_k u'_i} + \overline{U_k \rho' u'_i} + \overline{\rho' u'_k u'_i}] \\
&- U_{i,k} [\overline{\rho u'_k T'} + \overline{U_k \rho' T'} + \overline{\rho' u'_k T'}] \\
&- \overline{\rho u'_k (u'_i T')_{,k}} - \overline{U_k \rho' (u'_i T')_{,k}} - \overline{\rho' u'_k (u'_i T')_{,k}} \\
&+ \frac{\gamma}{Pr Re} [\overline{\kappa u'_i T'_{,kk}} + \overline{\kappa' u'_i T'_{,kk}} + \overline{\kappa' u'_i T'_{,kk}}] \\
&+ \Phi_p + \Phi_H
\end{aligned} \tag{4.6}$$

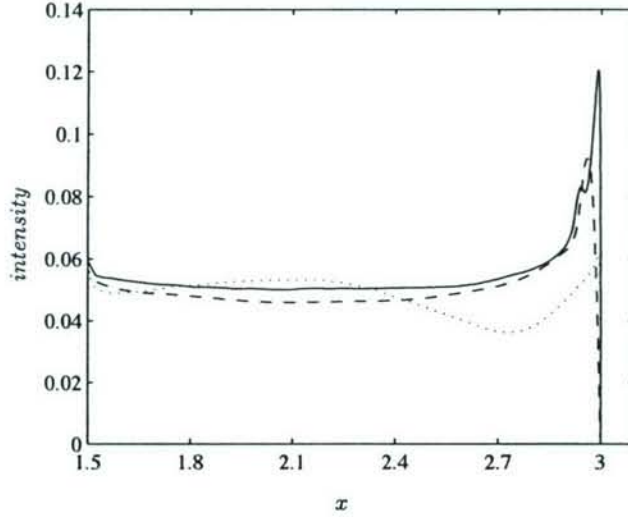


FIGURE 11. Turbulence intensity along the stagnation streamline. -----: u_{rms} ,: v_{rms} ,
 ———: w_{rms}

On the right hand side of (4.6), the first row is the temperature pressure gradient correlation; the second and the third rows are the heat flux production; the fourth row is the turbulence convection and the fifth row is the turbulent heat conduction. In the last row, Φ_p and Φ_H are the pressure dilatation work and viscous dissipation. The expressions for Φ_p and Φ_H are omitted here; they are not important in the present flow.

4.5. Turbulence intensity along the stagnation streamline

The change of the different components of turbulence intensity characterizes the anisotropy of stagnating turbulence. The root-mean-square value of velocity fluctuation along the stagnation streamline is shown in figure 11. The combination of the the turbulence length scale and the close location of the inflow boundary largely eliminates the free decaying stage of the free-stream turbulence. After a relatively balanced, isotropic development before $x \sim 2.4$, the turbulence develops strong anisotropy between $x \sim 2.4$ and 2.7. Within this region, both u_{rms} and w_{rms} increase but v_{rms} decreases, which is consistent with the prediction of RDT (Hunt 1973), indicating that the dominant mechanism for

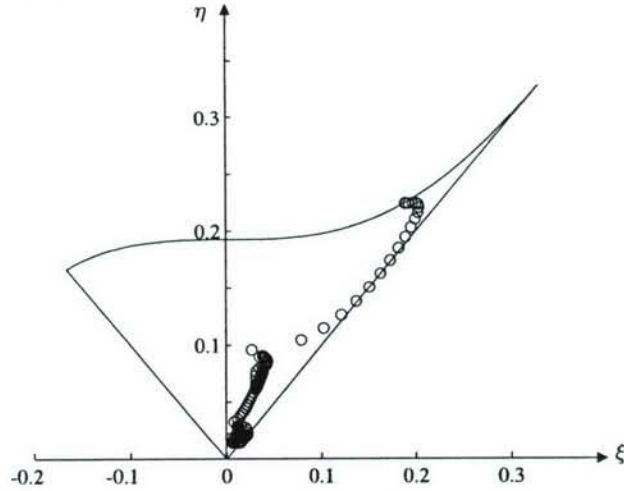


FIGURE 12. The evolution of the Reynolds-stress invariants along the stagnation streamline.

the turbulence anisotropy is by vortex stretching (Lee & Reynolds 1985) in y direction. At closer distances $x > 2.7$, the presence of the model surface generates a pronounced inviscid blocking effect. By the non-penetration boundary condition, the normal velocity, u_{rms} , must vanish at the wall. This causes u_{rms} to decay over a distance on the order of the turbulence integral length scale, typically larger than the boundary layer thickness. As a result, the kinetic energy of u_{rms} is partially redistributed into v and w components, leading to not only a further increase in w_{rms} , but also an increase in v_{rms} that was previously decreasing. Within an extremely close distance to the wall, viscous effect dominates and all the turbulence vanishes on the wall. The evolution of the turbulence anisotropy may also be characterized by the trajectory in the plane of the invariants ξ and η , here $\xi = (III_b/2)^{1/3}$, $\eta = (-II_b/3)^{1/2}$, and II_b and III_b are the second and third invariants of the Reynolds stress anisotropy tensor $b_{ij} = \overline{u_i u_j} / \overline{u_k u_k} - \delta_{ij}/3$ (Pope 2000). This is shown in figure 12 by the discrete dots representing different locations along the stagnation streamline. It can be seen that from a nearly isotropic state the Reynolds stress anisotropy develops as the stagnation point is approached and reaches a peak value

$\eta = 0.225$ inside the boundary layer. The turning point around $\eta = 0.1$ corresponds to the peak location of u_{rms} in figure 11, demarcating the beginning of significant inviscid blocking effect.

4.6. Turbulence budgets along the stagnation streamline

The budgets for the normal Reynolds stresses, $\overline{u'^2}$, $\overline{v'^2}$ and $\overline{w'^2}$, along the stagnation streamline are shown in figure 13. In these figures, the total dissipation Φ_T is used as the dissipation term. For $\overline{u'^2}$, the production term $-\overline{u'^2}\partial U/\partial x$ is associated with the mean flow strain rate, representing an energy transfer from the mean flow to $\overline{u'^2}$. Conversely, the production for $\overline{v'^2}$ is $\overline{v'^2}\partial V/\partial y$, which has an opposite sign and represents an energy transfer back to the mean flow. There is no production term for $\overline{w'^2}$ because the mean flow is two dimensional. The turbulence transport has the largest magnitude in $\overline{u'^2}$ but is confined mostly in the near wall region. It changes sign as the wall is approached, and if integrated along the stagnation line, it results a vanishing net contribution to the turbulence energy. Turbulent convection is not important for $\overline{v'^2}$ as compared to other terms. For $\overline{w'^2}$, we found that the turbulent convection term largely cancels with the mean convection term, and the sum of these two exerts a weak dissipative effect on $\overline{w'^2}$. The total dissipation extends farthest from the wall for $\overline{u'^2}$ and closest for $\overline{v'^2}$. It has the largest value for $\overline{w'^2}$, yet the smallest for $\overline{u'^2}$. Except for $\overline{w'^2}$, the dissipation term does not play a significant role along the stagnation line except extremely close to the wall for $\overline{v'^2}$.

Of particular interest for the stagnating turbulence is the redistribution term, i.e. the correlation between velocity and pressure gradient. Along the stagnation streamline, it is comparable in magnitude for all three normal Reynolds stresses. In strain-dominated flows, its primary effect is the generation of turbulence anisotropy. Being largely negative in figure 13a for $\overline{u'^2}$, it is positive for $\overline{v'^2}$ and $\overline{w'^2}$, as shown in figure 13b and 13c. Hence,

It represents a redistribution of the energy from $\overline{u'^2}$ to $\overline{v'^2}$ and $\overline{w'^2}$. In fact, for $\overline{v'^2}$ and $\overline{w'^2}$, it is the only major energy input. For $\overline{v'^2}$, it balances with the negative production term, whereas for $\overline{w'^2}$, the balance is with viscous dissipation and the total convection.

It is instructive to compare the energy redistribution obtained by the present LES and those by Reynolds Averaged Navier-Stokes (RANS) simulations. In the RANS simulations of Im *et al.* (2002), three Reynolds stress models, GL, GL-CL and SSG model, along with the conventional $k - \epsilon$ model, are used to compute impinging and counter-current jets. It is shown that in the strain-dominated flows, the overall predicative capability of the Reynolds stress models depends crucially on the correct modeling of the pressure strain correlation, which is part of the redistributive velocity pressure-gradient term. Thus in section 5 we will examine the eddy viscosity and the pressure strain correlation from the present LES and compare them with the corresponding the Reynolds stress models.

4.7. Fluctuations in local $s - n$ coordinates

Using the local $s - n$ coordinates, the profiles of $\overline{u_s'^2}$, $\overline{u_n'^2}$ and $\overline{w'^2}$ at $s/D = 0, 0.2, 0.8, 1.6$ are plotted in figure 14. The local boundary layer thickness at the corresponding locations are also marked on the right. Note that because of the symmetry at the stagnation streamline, the profile of $\overline{u'^2}$ is actually shown in figure 14a as $\overline{u_n'^2}$ (at $s = 0$), whereas the $\overline{u_s'^2}$ at $s = 0$ in figure 14a is actually $\overline{v'^2}$. This correspondence holds only along the stagnation streamline.

Near stagnation point $s = 0$, the magnitude of streamwise fluctuation is small because it corresponds to the velocity fluctuation in the axial direction of the strongly stretched vortices. At locations $s > 0$, however, the streamwise vortices become embedded in the mean boundary layer shear flow, therefore capable of generating large streamwise momentum exchange in the wall normal direction. This is demonstrated by the increase

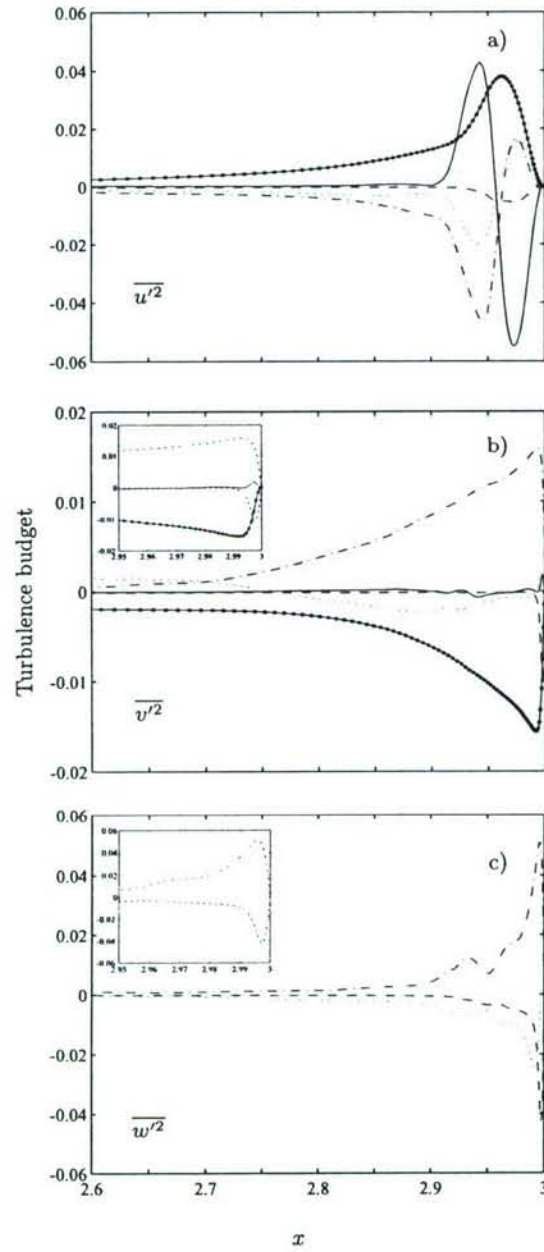


FIGURE 13. Turbulence budget along the stagnation streamline. a) $\overline{u'^2}$, —○—: production, -----: dissipation,: mean convection, ———: turbulent convection, —·—: velocity pressure gradient correlation. b) $\overline{v'^2}$, —○—: production, -----: dissipation,: mean convection, ———: turbulent convection, —·—: velocity pressure gradient correlation. c) $\overline{w'^2}$, -----: dissipation,: mean convection + turbulent convection, —·—: velocity pressure gradient correlation.

of the magnitude of $\overline{u_s'^2}$ as one moves downstream. Also notice that the peak of $\overline{u_s'^2}$ measured in local boundary layer thickness is getting closer to the wall at downstream, showing the characteristics of a transitional boundary layer.

The $\overline{u_n'^2}$ shows its highest peak value at $s = 0$ where the vortex stretching is strongest, and then decreases downstream. It becomes significantly smaller than the streamwise fluctuation $\overline{u_s'^2}$ at the downstream locations, indicating that the turbulence there is mainly dominated by strong shear. Moreover, figure 14b also demonstrates the wall blocking effect extending to a distance on the order of turbulence integral scale, which explains the peaks of $\overline{u_n'^2}$ outside of the boundary layer.

For the spanwise fluctuation $\overline{w'^2}$, figure 14c shows that its amplitude also decays monotonically downstream from the stagnation point. As mentioned before, the strong mean flow straining and wall blocking effects decrease as one moves downstream, and the flow gradually changes to a shear-dominated type. In such cases, the redistribution term plays a much smaller role in transferring the turbulence kinetic energy from $\overline{u'^2}$ to $\overline{w'^2}$, yet there is no production term for $\overline{w'^2}$. The combination of these factors determines the trend of the decreasing $\overline{w'^2}$ in streamwise direction. Another feature of the $\overline{w'^2}$ profile is that besides the main peak inside the boundary layer, a second peak develops outside the boundary layer in the leading edge region ($s/D < 0.8$). We believe that this is yet another indication of the turbulence anisotropy resulting from the existence of the strong streamwise vortices. Far from the leading edge, the free-stream turbulence is isotropic, and the turbulence vortices are orientated randomly with no preferred direction. As it approaches the stagnation point, turbulence anisotropy develops because of the strong streamwise vortices emerging from the background turbulence. If these vortices were perfectly stationary then they would appear in the mean-flow, but they are induced by free-stream turbulence and thus form and decay and move about as well. One of the

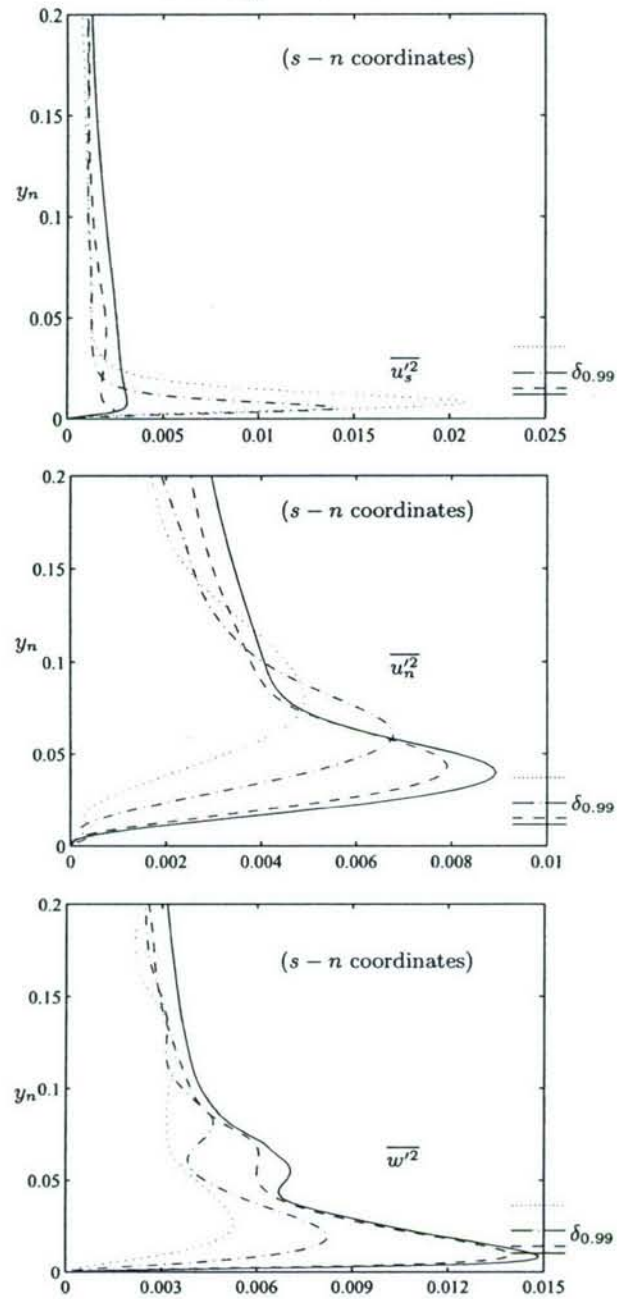


FIGURE 14. The profiles of tangential, normal and spanwise velocity fluctuation at different streamwise locations. The corresponding laminar boundary layer thickness $\delta_{0.99}$ is marked on the right. —: $s = 0$, - - - -: $s = 0.2D$, - · - ·: $s = 0.8D$, and · · · ·: $s = 1.6D$.

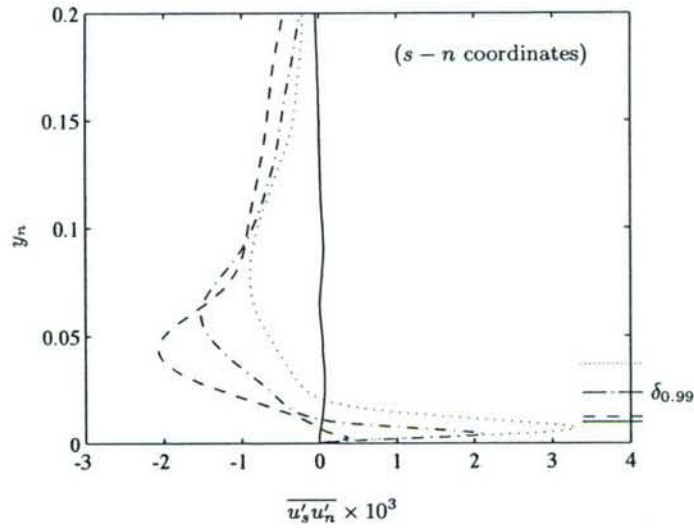


FIGURE 15. The profiles of turbulent Reynolds stress $\overline{u'_s u'_n}$ at different streamwise locations. The corresponding laminar boundary layer thickness $\delta_{0.99}$ is marked on the right. —: $s = 0$, - - - -: $s = 0.2D$, — · — ·: $s = 0.8D$, and · · · ·: $s = 1.6D$.

characteristics of the streamwise vortices is that the spanwise velocity w changes sign across the vortex section, and thus its root-mean-square value has a two-peak structure with the lowest point in between corresponding to the vortex center. The two peaks are not of equal strength, since the magnitude of w' is increasing. When these streamwise vortices become strong and frequent enough, this particular pattern, super-imposed on the background turbulence field, gives rise to the second peak in the overall w'_{rms} .

The only significant shear stress in the present flow is $\overline{u'v'}$ and it vanishes on the stagnation streamline due to the symmetry in velocity u and v . In figure 15 the profiles of $\overline{u'_s u'_n}$ are plotted in local $s - n$ coordinates. There are two distinct peaks for each curve, one being negative outside the boundary layer, and the other positive inside the boundary layer. Moving downstream from the stagnation point, one finds the amplitude of the outer peak decreases whereas the amplitude of the inner peak increases. The inner positive peak of $\overline{u'_s u'_n}$ represents a counter-gradient hence nonlocal transport of momen-

tum, and this is believed to be a result of vortex rebounding at the wall. Essentially, mean convection brings the stretched turbulence eddies from free-stream into the laminar boundary layer and aligns the vortices in streamwise direction. As these streamwise vortices approach the wall, the no-slip wall boundary condition enforces two thin regions of large vorticity (with opposite sign to the approaching vortices) to be generated between the wall and the approaching vortices. When the streamwise vortices are strong enough, the thin underneath region can be lifted up and forms a dipole vortex with the primary vortex. This newly formed dipole vortex induces a positive normal velocity and the vortex bounces back from the wall. The mechanism of rebounding vortex has been previously studied in detail using a pair of counter rotating vortices, or a dipole vortex, colliding with a wall under self-induced velocity (Orlandi 1990; Carnevale *et al.* 1997). Here in the leading edge region, the vortices are convected by the mean flow (thus a vortex pair is not needed), but the vortex-wall interaction is similar. In terms of fluctuation velocity, when turbulence is brought into boundary layer from the free-stream, it creates a region of $u'_s > 0, u'_n < 0$ within the boundary layer which is responsible for the overall negative $\overline{u'_s u'_n}$. However, because of the vortex rebounding, the normal velocity u'_n changes sign in the near wall region and consequently generates the positive value of $\overline{u'_s u'_n}$.

4.8. Thermal fluxes $\overline{u'_s T'}$ and $\overline{u'_n T'}$

The profiles of the thermal fluxes $\overline{u'_s T'}$ and $\overline{u'_n T'}$ are shown in figure 16 and 17 at different streamwise locations. While the tangential flux $\overline{u'_s T'}$ increases as one moves downstream, the peak value of the positive normal flux $\overline{u'_n T'}$ decreases. Near the stagnation point, the $\overline{u'_n T'}$ is predominantly positive due to the same free-stream turbulence impingement that gives rise to the negative shear stress $\overline{u'_s u'_n}$. Different from that of the $\overline{u'_s u'_n}$, however, is the peak location of the $\overline{u'_n T'}$. Comparing figure 17 and 15, one can see the positive peak

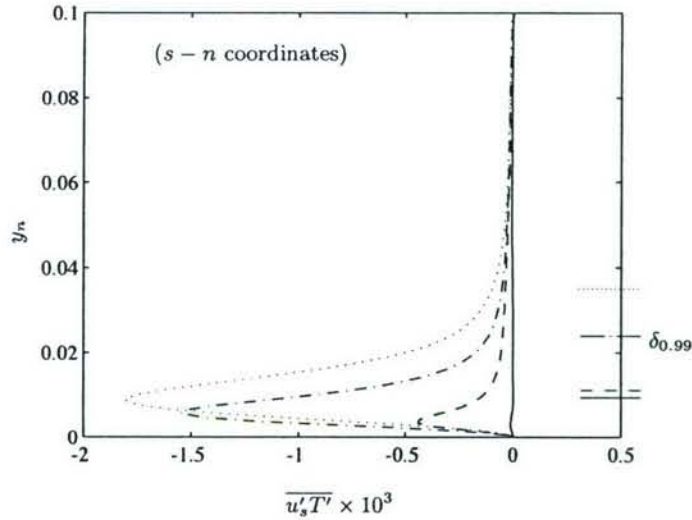


FIGURE 16. The profiles of tangential heat flux $\overline{u'_s T'}$ at different streamwise locations. The corresponding laminar boundary layer thickness $\delta_{0.99}$ is marked on the right. —: $s = 0$, - - - -: $s = 0.2D$, — · —: $s = 0.8D$, and · · · ·: $s = 1.6D$.

of $\overline{u'_n T'}$ is almost five times closer to the wall than the negative peak of $\overline{u'_s u'_n}$. We believe this difference in the peak locations between the thermal flux and the shear stress explains the greater sensitivity to the free-stream turbulence for the heat transfer rate than the wall friction coefficient, as observed in figure 4. Close to the wall at downstream locations, $\overline{u'_n T'}$ changes sign, indicating the similar counter-gradient feature in the thermal fluxes. The mechanism can be understood in a similar way through the vortex rebound as for $\overline{u'_s u'_n}$ discussed in the last subsection. The profiles of the production terms for $\overline{u' T'}$ and $\overline{v' T'}$ are shown in figures 18 and 19. Along the streamwise direction, the $\overline{u' T'}$ increases but $\overline{v' T'}$ decreases. The decaying of the production in $\overline{v' T'}$ may be attributed to the difference in the peak locations of the fluctuation velocity v' and temperature T' . The former shifts away from the wall at downstream while the latter remains close to the wall in the entire streamwise range.

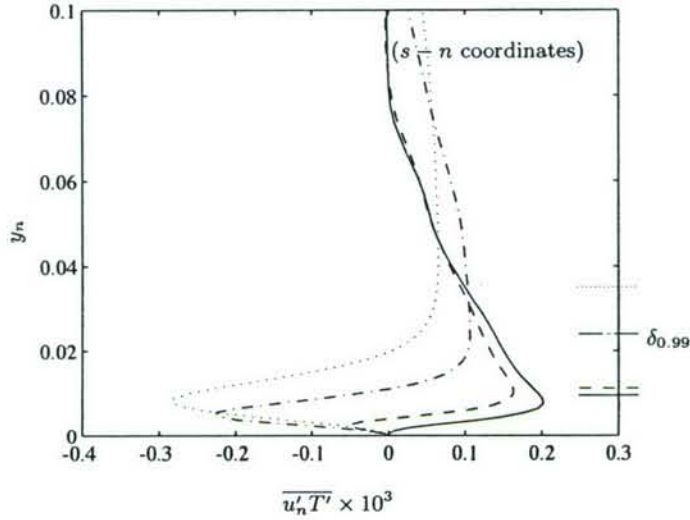


FIGURE 17. The profiles of wall normal heat flux $\overline{u'_n T'}$ at different streamwise locations. The corresponding laminar boundary layer thickness $\delta_{0.99}$ is marked on the right. —: $s = 0$, - - - -: $s = 0.2D$, — · —: $s = 0.8D$, and · · · ·: $s = 1.6D$.

5. Eddy viscosity and pressure-strain correlation

As mentioned in the introduction, modelling turbulence effects in strain dominated flows remains a challenging problem. One of the primary goals of the present LES study is to provide useful information for this effort. Conventional two equation models do not address the anisotropy of stagnating turbulence, and the use of linear constitutive model, $\overline{u'_i u'_j} = -2\nu_T S_{ij} + 2/3k\delta_{ij}$, results in severe over prediction of the turbulence production. In order to recover the correct turbulence production, one remedy (Durbin 1996) based on realizability consideration introduces an upper bound on the eddy viscosity, $\nu_T \leq \frac{k}{\sqrt{6}|S|}$, where $|S|$ is the magnitude of the strain rate. In practice, the constraint can also be expressed in terms of turbulence time scale T by using formula $\nu_T = C_\mu kT$. For example, $T = \min\{\frac{k}{\epsilon}, \frac{\alpha}{\sqrt{6}C_\mu|S|}\}$, where $\alpha = 0.6$, has been incorporated into standard $k - \epsilon$ model to compute turbine blade heat transfer (Medic & Durbin 2002). For the realizability condition, figure 20 shows the normalized turbulence eddy viscosity ν_T (not the SGS

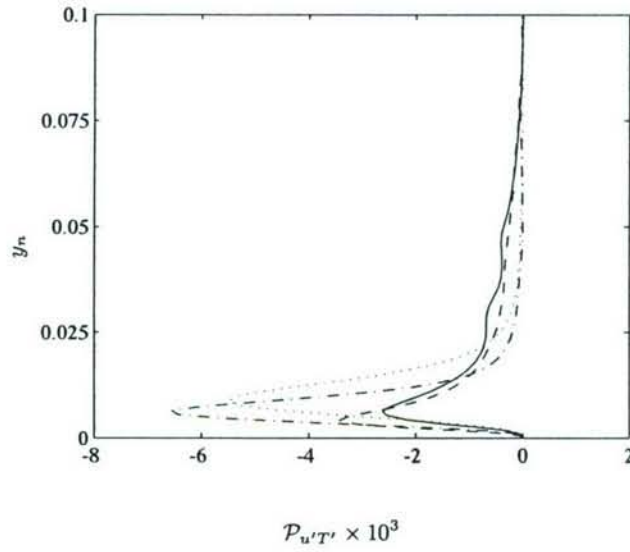


FIGURE 18. Profiles of turbulence production for $\overline{u'T'}$ along wall normal direction. —: $s = 0$, - - - - -: $s = 0.2D$, — · — ·: $s = 0.8D$, and · · · · ·: $s = 1.6D$.

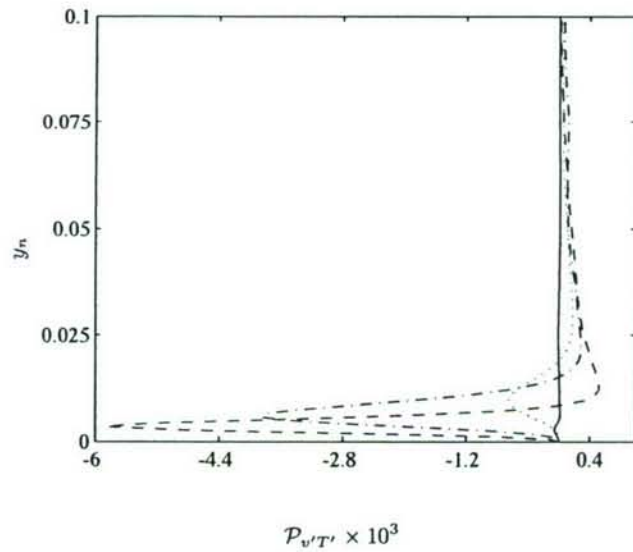


FIGURE 19. Profiles of turbulence production for $\overline{v'T'}$ along wall normal direction. —: $s = 0$, - - - - -: $s = 0.2D$, — · — ·: $s = 0.8D$, and · · · · ·: $s = 1.6D$.

eddy viscosity) and the corresponding $\nu_{TR} = \frac{k}{\sqrt{6}|S|}$ along the stagnation line based on the present LES results. The effective ν_T is obtained through $\mathcal{P} = 2\nu_T S_{ij} S_{ij}$ with

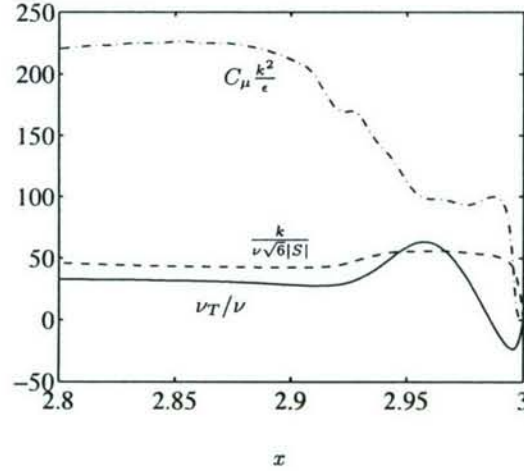


FIGURE 20. Turbulence eddy viscosity ν_T (not the SGS ν_T). —: LES results, — — —: $k - \epsilon$ model, - · - · -: realizability constraint.

the turbulence production \mathcal{P} and strain rate S_{ij} computed from the LES results. As a comparison, the eddy viscosity obtained using the conventional $k - \epsilon$ model $\nu_{Tk} = C_\mu k^2/\epsilon$, $C_\mu = 0.09$ is also plotted. Away from the stagnation point, the value of ν_{Tk} is about five times of ν_T . Close to the stagnation point, ν_{Tk} decreases and approaches to a constant value about two times of ν_T . Because of this elevated eddy viscosity, the $k - \epsilon$ model overpredicts the turbulence production in stagnation point flows. On the other hand, the eddy viscosity ν_{TR} tracks the ν_T quite well and provides a useful upper bound for ν_T , indicating the effectiveness of the realizability constraints.

In second-order Reynolds stress models, the pressure-strain correlation

$$\phi_{ij} = \frac{p'}{\rho} \left(\frac{\partial u_i}{\partial x_j} + \frac{\partial u_j}{\partial x_i} \right) \quad (5.1)$$

is the primary means to redistribute the kinetic energy among different components of the Reynolds stresses. The current LES results can be used to examine the particular pressure-strain correlations in different Reynolds stress models. Here three of such turbulence models are chosen that were used in Im *et al.* (2002): the GL (with wall reflection

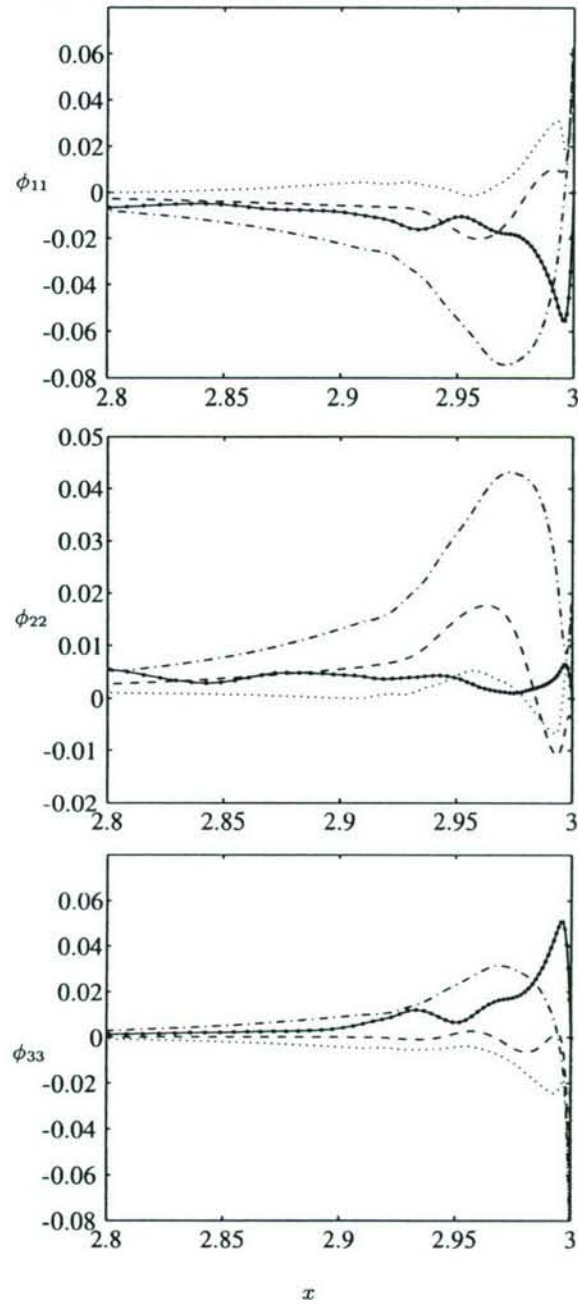


FIGURE 21. The pressure-strain correlation $\phi_{\alpha\alpha} = \overline{\frac{p'}{\rho} \frac{\partial u_\alpha}{\partial x_\alpha}}$ (no summation over α) along the stagnation streamline, comparison between the LES results and different Reynolds stress models. —○—: LES, ·····: GL model, — — —: GL-CL model, - - - - -: SSG model.

terms), GL-CL and SSG models. Figure 21 shows the comparison of the $\phi_{\alpha\alpha}$ along the stagnation streamline between the LES results and the turbulence models (see Appendix B for the expressions of $\phi_{\alpha\alpha}$ in these models). First notice that in the region close to the stagnation point the GL model predicts all three components of $\phi_{\alpha\alpha}$ with the wrong sign. Between the GL-CL and the SSG models, the GL-CL is significantly better in predicting ϕ_{11} and ϕ_{33} ; not only the sign is more consistent, the magnitudes are also comparable to the LES results. The LES data show the ϕ_{22} is smaller than the other two components, this is however not apparent in the model predictions. Both GL-CL and SSG models severely overpredict ϕ_{22} with the GL-CL model having the largest error albeit a more consistent sign. Another feature about the GL-CL model is that the peaks of the $\phi_{\alpha\alpha}$ are located at a larger distance from the wall than the LES results. These findings are consistent with the observations made by Im *et al.* (2002) from the RANS calculations and suggest that the GL-CL model is the overall most effective among the three turbulence models for stagnation point type or strain dominated flows.

6. Concluding remarks

In this paper, the stagnation point flow and heat transfer at an elliptical isothermal leading edge in the presence of free-stream turbulence is investigated using LES. Along the stagnation streamline, the turbulence intensity in streamwise (x) and spanwise (z) directions increases whereas the intensity in transverse (y) direction decreases. Very close to the wall, the streamwise fluctuation is reduced by the wall blockage effect, and its energy is transferred to the other two components. As a result, the spanwise turbulence intensity becomes the most dominant among the three components in this region. The most important Reynolds stress budget terms for the stagnating turbulence are the production and the velocity pressure gradient correlation. In particular, the latter dominates

the development of the transverse and spanwise normal Reynolds stresses, and hence the turbulence anisotropy. The boundary layer under free-stream turbulence is found to be in non-equilibrium and pre-transitional. The normal turbulence heat flux is shown to have a peak location much closer to the wall than that for the Reynolds shear stress, explaining the greater sensitivity to free-stream turbulence for the heat transfer than the momentum transfer in stagnation point flows.

Intense, streamwise vortical structures generated at the leading edge due to strong vortex stretching are found to be the direct cause of the heat transfer enhancement. These vortices have a spanwise dimension about $2 \sim 3$ times the local boundary layer thickness and they move laterally at a speed comparable to the local spanwise fluctuation velocity. The enhancement of the heat transfer obtained by the present LES agree well with the corresponding experimental measurements.

The LES results are used to examine the eddy viscosity obtained from the conventional $k - \epsilon$ model and from realizability conditions. The $k - \epsilon$ model is found to produce excessive turbulent eddy viscosity in stagnation point flows, but the realizability condition provides an adequate upper bound for the eddy viscosity. Furthermore, the pressure-strain correlations obtained by the present LES are compared with those from three Reynolds stress models (GL, GL-CL and SSG). Among the three models, it is found that the GL-CL model provides the most effective pressure strain correlations in stagnation point or strain dominated flows. It is hoped that the LES data will be useful in developing improved models of pressure-strain correlations for strain-dominated flows.

Acknowledgments

This work was supported by the Air Force Office of Scientific Research under grant No. F49620-01-1-0138 with Dr. Tom Beutner as the program manager. The computer resource was provided by DoD Major Shared Resource Center at U.S. Army Engineer Research

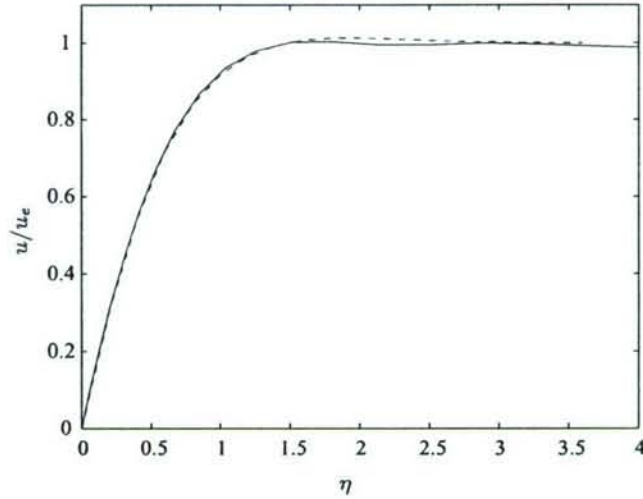


FIGURE 22. Comparison of boundary layer velocity profile at the leading edge. $Re = 10^5$, $M = 0.15$, $T_w/T_0 = 2.0$, $Pr = 1.0$.——: computation, - - - - -: similarity solution

and Development Center, and Army Research Laboratory. We appreciate the referee's comments on the original manuscript, particularly those concerning the Reynolds stress models.

Appendix A. Validation

Laminar compressible boundary layer profiles at the leading edge allow self-similar analytic solutions when viscosity varies as a linear function of temperature (Reshotko & Beckwith 1957). Figures 22 to 23 show the velocity and enthalpy profiles for $Pr = 1$ for flow over an elliptical leading edge. The wall temperature is set to be twice the total temperature of the incoming flow, i.e. $T_w/T_0 = 2$. For different Mach numbers, $Ma = 0.1$ and $Ma = 0.8$ (not shown here), excellent agreement in the velocity and enthalpy profiles is obtained between the numerical and analytical solution. Further comparisons at different flow conditions can be found in Xiong (2004). To validate the code in unsteady computations, we choose to compute the boundary layer receptivity to ambient sound at a blunt leading edge. Receptivity is defined as a process by which external flow disturbances

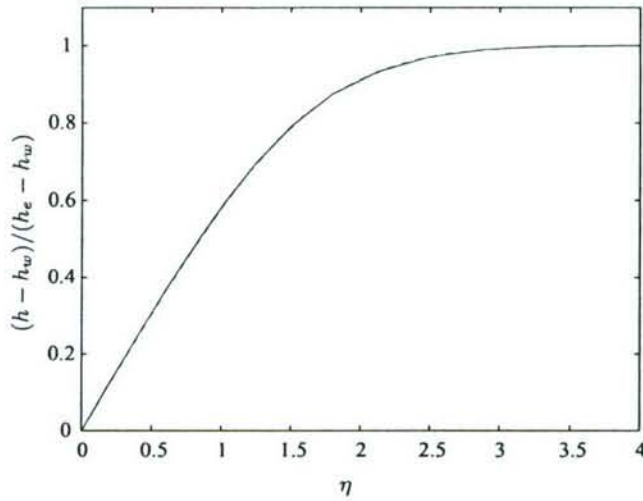


FIGURE 23. Comparison of boundary layer enthalpy profile at the leading edge. $Re = 10^5$, $M = 0.15$, $T_w/T_0=2.0$, $Pr = 1.0$. —: computation, - - - - -: similarity solution

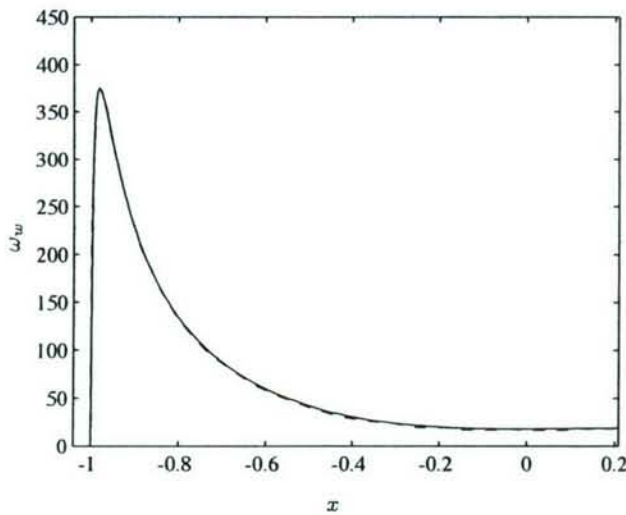


FIGURE 24. Comparison of the wall vorticity ω_{wall} . —, present computation, - - - - -, result of Collis (1997).

are converted into instability waves (Morkovin 1969). For the flat plate boundary layer flow, the sound receptivity refers to the generation of T-S instability waves inside the boundary layer by free-stream acoustic waves. We use the same flow configuration as in Lin (1992) and Collis (1997) for a compressible boundary layer on a flat plate with a

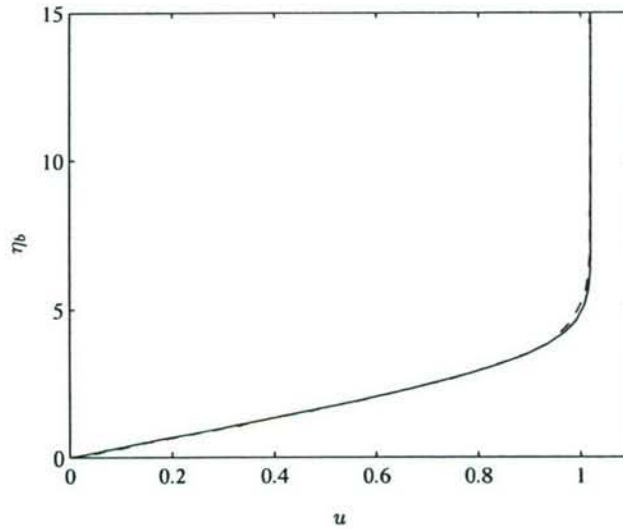


FIGURE 25. Streamwise velocity profile at $x = 2.783$. —, present computation, ----, result of Collis (1997).

super ellipse leading edge. However, unlike the usual numerical receptivity studies, which is based on linearized governing equations about a base flow, we use the full nonlinear N-S equations to compute both the base and the disturbed flows. The evolution of the disturbance is obtained by subtracting the base solution from the instantaneous solution. In the present computation, the mean flow is judged to be steady after the residue has dropped by 8 orders of magnitude from its initial value. The mean flow wall vorticity ω_w is shown in figure 24 and it is in very good agreement with those from Collis (1997). In figure 25, the streamwise velocity profile at $x = 2.783$ is shown as a function of the Blasius variable η_b , defined as $\eta_b = y\sqrt{Re/(x+1)}$. Again, the present result agrees well with Collis (1997).

Once the base flow is obtained, acoustic waves are introduced through the inflow sponge at a frequency $\omega = 3.312$ and amplitude $A = 0.001$ (see Xiong (2004) for details). With the mean flow Mach number $M = 0.1$, the downstream acoustic wave length is $\lambda_a = 20.833$.

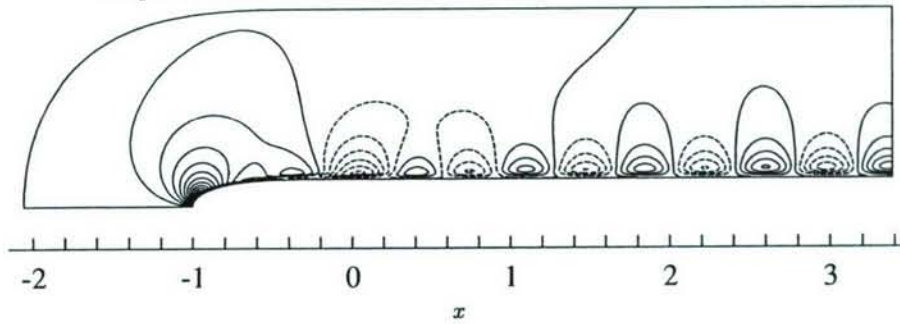


FIGURE 26. Disturbance vertical velocity fields of sound receptivity on a flat plate with a super-ellipse leading edge. Contour levels: $v_{max} = 1.17 \times 10^{-4}$, $v_{min} = -3.90 \times 10^{-4}$, $\Delta v = 8.16 \times 10^{-6}$.

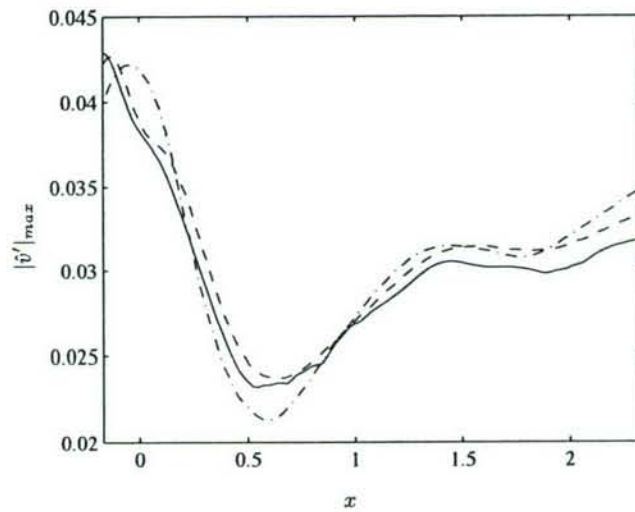


FIGURE 27. Local maximum of the amplitude of the T-S wave based on the vertical disturbance velocity. —: present computation. - - - - -: result of Collis (1997). - · - · -: result of Lin (1992).

The T-S wave field inside the boundary layer induced by the sound wave is plotted in figure 26 using the vertical velocity component. Notice the overall disturbance flow field in the boundary layer contains not only the excited T-S wave, but also the incoming and scattered acoustic waves.

After subtracting the acoustic components from the total disturbance solution follow-

ing Wlezien (1994), the amplitude of the T-S wave is shown in figure 27. The results from Lin (1992) (for incompressible flow) and from Collis (1997) are also shown. Again, we can see that the computations have followed similar shapes, with some small quantitative differences. Given the great sensitivity of the growth rate of the T-S wave, the difference is considered to be acceptable, and the overall agreement is satisfactory.

Appendix B. Pressure strain correlation

Let $\phi_{\alpha\alpha}$ denote the pressure strain correlation (no summation over α) in the equations for $\overline{u^2}$, $\overline{v^2}$ and $\overline{w^2}$,

$$\phi_{\alpha\alpha} = \frac{p'}{\rho} \frac{\partial u_\alpha}{\partial x_\alpha}, \quad (\text{B } 1)$$

and k and ϵ denote the turbulence kinetic energy and dissipation. Along the stagnation streamline, the $\phi_{\alpha\alpha}$ in the GL, GL-CL and SSG Reynolds stress models takes the following form :

GL model:

$$\phi_{11} = -\frac{\epsilon}{k} \left[\alpha_1 (\overline{u^2} - \frac{2}{3}k) + 2\alpha_{1w} \overline{u^2} f_n \right] - \frac{\alpha_2}{3} [(2P_{11} - P_{22}) - 2\beta_{2w}(2P_{11} - P_{22})f_n] \quad (\text{B } 2)$$

$$\phi_{22} = -\frac{\epsilon}{k} \left[\alpha_1 (\overline{v^2} - \frac{2}{3}k) - \alpha_{1w} \overline{u^2} f_n \right] - \frac{\alpha_2}{3} [(2P_{22} - P_{11}) + \beta_{2w}(2P_{11} - P_{22})f_n] \quad (\text{B } 3)$$

$$\phi_{33} = -\frac{\epsilon}{k} \left[\alpha_1 (\overline{w^2} - \frac{2}{3}k) - \alpha_{1w} \overline{u^2} f_n \right] + \frac{\alpha_2}{3} [(P_{11} + P_{22}) - \beta_{2w}(2P_{11} - P_{22})f_n] \quad (\text{B } 4)$$

GL-CL model:

$$\begin{aligned} \phi_{11} = & -\frac{\epsilon}{k} \left[\alpha_1 (\overline{u^2} - \frac{2}{3}k) + 2\alpha_{1w} \overline{u^2} f_n \right] - \frac{\alpha_2(2P_{11} - P_{22})}{3} \\ & - f_n [2(\gamma_{2w} + \gamma'_{2w})P_{11} + 2\gamma_{2w}P_{22} + \frac{2k(2\gamma'_{2w} - \gamma''_{2w})}{3} S_{11}] \end{aligned} \quad (\text{B } 5)$$

$$\begin{aligned} \phi_{22} = & -\frac{\epsilon}{k} \left[\alpha_1 (\overline{v^2} - \frac{2}{3}k) - \alpha_{1w} \overline{u^2} f_n \right] - \frac{\alpha_2(2P_{22} - P_{11})}{3} \\ & + f_n [(\gamma_{2w} + \gamma'_{2w})P_{11} + \gamma_{2w}P_{22} + \frac{k(2\gamma'_{2w} - \gamma''_{2w})}{3} S_{11}] \end{aligned} \quad (\text{B } 6)$$

$$\phi_{33} = -\frac{\epsilon}{k} \left[\alpha_1 (\overline{w^2} - \frac{2}{3}k) - \alpha_{1w} \overline{u^2} f_n \right] + \frac{\alpha_2(P_{11} + P_{22})}{3}$$

$$+f_n[(\gamma_{2w} + \gamma'_{2w})P_{11} + \gamma_{2w}P_{22} + \frac{k(2\gamma'_{2w} - \gamma''_{2w})}{3}S_{11}] \quad (\text{B } 7)$$

where

$$P_{11} = -\overline{u^2} \frac{\partial U}{\partial x}, \quad P_{22} = -\overline{v^2} \frac{\partial V}{\partial y}, \quad S_{11} = \frac{\partial U}{\partial x}, \quad S_{22} = \frac{\partial V}{\partial y}, \quad f_n = \frac{k^{3/2}}{\alpha_n \epsilon x_n}. \quad (\text{B } 8)$$

The coefficients are $\alpha_1 = 1.8$, $\alpha_2 = 0.6$, $\alpha_{1w} = 0.5$, $\beta_{2w} = 0.3$, $\gamma_{2w} = 0.08$, $\gamma'_{2w} = 0.1$, $\gamma''_{2w} = 0.4$, $\alpha_n = 2.5$. The x_n is the normal distance to the wall.

SSG model:

$$\begin{aligned} \phi_{11} = & -(\sigma_1 \epsilon + \sigma_1^* P)b_{11} + \sigma_2 \epsilon (b_{11}^2 - \frac{1}{3} \Pi_b) + (\sigma_3 - \sigma_3^* \Pi_b^{1/2})kS_{11} + \\ & \frac{2}{3} \sigma_4 k (2b_{11}S_{11} - b_{22}S_{22}) \end{aligned} \quad (\text{B } 9)$$

$$\begin{aligned} \phi_{22} = & -(\sigma_1 \epsilon + \sigma_1^* P)b_{22} + \sigma_2 \epsilon (b_{22}^2 - \frac{1}{3} \Pi_b) + (\sigma_3 - \sigma_3^* \Pi_b^{1/2})kS_{22} + \\ & \frac{2}{3} \sigma_4 k (2b_{22}S_{22} - b_{11}S_{11}) \end{aligned} \quad (\text{B } 10)$$

$$\phi_{33} = -(\sigma_1 \epsilon + \sigma_1^* P)b_{33} + \sigma_2 \epsilon (b_{33}^2 - \frac{1}{3} \Pi_b) - \frac{2}{3} \sigma_4 k (b_{11}S_{11} + b_{22}S_{22}) \quad (\text{B } 11)$$

where

$$P = P_{11} + P_{22}, \quad b_{ii} = \frac{\overline{u_i u_i}}{2k} - \frac{1}{3}, \quad \Pi_b = b_{ii}^2. \quad (\text{B } 12)$$

The coefficients are $\sigma_1 = 3.4$, $\sigma_1^* = 1.8$, $\sigma_2 = 4.2$, $\sigma_3 = 0.8$, $\sigma_3^* = 1.3$, $\sigma_4 = 1.25$.

REFERENCES

- AMES, F. E. & MOFFAT, R. J. 1990 Heat transfer with high intensity, large scale turbulence: The flat plate turbulent boundary layer and the cylindrical stagnation point. In *Dept. of Mech. Engng. Report No. HMT-44*. Stanford University, Stanford, CA.
- BAE, S., LELE, S. K. & SUNG, H. J. 2000 Influence of inflow disturbances on stagnation-region heat transfer. *ASME Journal of Heat Transfer* **122**, 258–265.
- BARDINA, J., HUANG, P. G. & COAKLEY, T. J. 1997 Turbulence modeling validation. *AIAA Paper 97-2121*.

- CARNEVALE, G., FUENTES, O. V. & ORLANDI, P. 1997 Inviscid dipole-vortex rebound from a wall or coast. *J. Fluid Mech.* **351**, 75–103.
- CHAMPION, M. & LIBBY, P. A. 1991 Asymptotic analysis of stagnating turbulent flows. *AIAA Journal* **29** (1), 16–24.
- CHAMPION, M. & LIBBY, P. A. 1994 Reynolds stress description of opposed and impinging turbulent jets ii. axisymmetric jets impinging on nearby walls. *Physics of Fluids* **6** (5), 1805–1819.
- COLLIS, S. S. 1997 A computational investigation of receptivity in high-speed flow near a swept leading-edge. PhD thesis, Stanford University.
- CRAFT, T. J., GRAHAM, L. J. W. & LAUNDER, B. E. 1993 Impinging jet studies for turbulence model assessment—ii. an examination of the performance of four turbulence models. *Int. J. Heat Mass Transf.* **36** (10), 2685–2697.
- DULLENKOPF, K. & MAYLE, R. E. 1995 An account of free-stream-turbulence length scale on laminar heat transfer. *ASME Journal of Turbomachinery* **117**, 401–406.
- DURBIN, P. 1996 On the $k-\epsilon$ stagnation point anomaly. *Int. J. Heat and Fluid Flow* **17**, 89–90.
- EISEMAN, P. 1985 Grid generation for fluid mechanics. *Ann. Rev. Fluid Mech.* **17**, 487–522.
- GIBSON, M. M. & LAUNDER, B. E. 1978 Ground effects on pressure fluctuation in the atmospheric boundary layer. *J. Fluid Mech.* **86**, 491–591.
- GIEDT, W. H. 1949 Investigation of variation of point unit heat transfer coefficient around a cylinder normal to an airstream. *Trans. ASME* **71** pp. 375–381.
- GÖRTLER, H. 1955 Three dimensional instability of the plane stagnation flow with respect to vortical disturbance. In *Fifty years of boundary layer research* (ed. H. Görtler & W. Tollmien), pp. 304–314. Vieweg and Sohn, Braunschweig.
- HÄMMERLIN, G. 1955 On instability theory of plane stagnation point flow. In *Fifty years of boundary layer research* (ed. H. Görtler & W. Tollmien), pp. 315–327. Vieweg and Sohn, Braunschweig.
- HEGGE-ZIJNEN, B. G. V. D. 1957 Heat transfer from horizontal cylinders to a turbulent air flow. *Appl. Sci. Res. A* **7**, 205–223.

- HUNT, J. C. R. 1973 A theory of turbulent flow round two-dimensional bluff bodies. *J. Fluid Mech.* **61**, 625–706.
- IM, Y. H., HUH, K. Y. & KIM, K.-Y. 2002 Analysis of impinging and countercurrent stagnating flows by Reynolds stress model. *ASME J. Fluid Engineering* **124**, 706–718.
- ISHIGAKI, M. 1970 Periodic boundary layer near a two-dimensional stagnation point. *J. Fluid Mech.* **43**, 477–486.
- KESTIN, J., MAEDER, P. F. & SOGIN, H. H. 1961 The influence of turbulence on the transfer of heat to cylinders near the stagnation point. *ZAMP* **12**, 115–132.
- KESTIN, J. & WOOD, R. T. 1970 On the stability of two-dimensional stagnation flow. *J. Fluid Mech.* **44**, 461–479.
- KESTIN, J. & WOOD, R. T. 1971 The influence of turbulence on mass transfer from cylinders. *ASME J. Heat Transfer* **93C**, 321–327.
- LEE, M. J. & REYNOLDS, W. C. 1985 Numerical experiments on the structure of homogeneous turbulence. TF Report 24. Stanford University.
- LIGHTHILL, M. J. 1954 The response of laminar skin friction and heat transfer to fluctuations in the stream velocity. *Proc. Roy. Soc. A* **224**, 1–23.
- LIN, N. 1992 Receptivity of the boundary layer over a flat plate with different leading-edge geometries: Numerical simulations. PhD thesis, Arizona State University.
- LIN, R. S. & MALIK, M. R. 1996 On the stability of attachment-line boundary layers. Part 1. the incompressible swept Himenz flow. *J. Fluid Mech.* **311**, 239–255.
- LOWERY, G. W. & VACHON, R. I. 1975 Effect of turbulence on heat transfer from heated cylinders. *Int. J. Heat Mass Transfer* **18** (No. 11), 1229–1242.
- LUI, C. 2003 A numerical investigation of shock associated noise. PhD thesis, Stanford University.
- LYELL, M. J. & HUERRE, P. 1985 Linear and nonlinear stability of plane stagnation flow. *J. Fluid Mech.* **161**, 295–312.
- MEDIC, G. & DURBIN, P. A. 2002 Toward improved prediction of heat transfer on turbine blades. *ASME J. of Turbomachinery* **124**, 187–192.

- MEHENDALE, A. B., HAN, J. C. & OU, S. 1991 Influence of high mainstream turbulence on leading edge heat transfer. *ASME Journal of Heat Transfer* **113**, 843–850.
- MERCHANT, G. J. & DAVIS, S. H. 1989 Modulated stagnation-point flow and steady streaming. *J. Fluid Mech.* **198**, 543–555.
- MOIN, P., SQUIRES, K., CABOT, W. & S.LEE 1991 A dynamic subgrid-scal model for compressible turbulence and scalar transport. *Physics of Fluids* **A3** (11), 2746–2757.
- MORKOVIN, M. V. 1969 Bypass-transition research: issues and philosophy. *Tech. Rep. Tech. Rep. AFFDL-TR-68-149*. Air Force Flight Dynamics laboratory, Wright-Paterson Air Force Base.
- MORKOVIN, M. V. 1979 On the question of instabilities upstream of cylindrical bodies. *NASA Contractor Report* **3231**.
- ORLANDI, P. 1990 Vortex dipole rebound from a wall. *Physics of Fluids* **A 2**, 1429–1436.
- PEDLEY, T. J. 1972 Two-dimensional boundary layers in a free stream which oscillates without reversing. *J. Fluid Mech.* **55**, 359–383.
- PIERCY, N. A. V. & RICHARDSON, E. G. 1928 The variation of velocity amplitude close to the surface of a cylinder moving through a viscous fluid. *Phil. Mag. Series 7* **6**, 970–977.
- PIERCY, N. A. V. & RICHARDSON, E. G. 1930 The turbulence in front of a body moving through a viscous fluid. *Phil. Mag. Series 7* **9**, 1038–1041.
- POPE, S. B. 2000 *Turbulent Flows*. Cambridge, UK: Cambridge University Press.
- RESHOTKO, E. & BECKWITH, I. E. 1957 Compressible laminar boundary layer over a yawed infinite cylinder with heat transfer and arbitrary prandtl number. Report 1379. NACA.
- SMITH, M. C. & KUETHE, A. M. 1966 Effects of turbulence on laminar skin friction and heat transfer. *Phys. Fluids* **9** (No. 12), 2337–2344.
- SPALART, P. R. 1989 Direct numerical study of leading-edge contamination. *AGARDC* **438** (5.1-5.13), 457–468.
- SPALART, P. R. & ALLMARAS, S. R. 1992 A one-equation turbulence model for aerodynamic flows. *AIAA paper 92-0439*.
- SPEZIALE, C. G., SARKAR, S. & GATSKI, T. B. 1991 Modelling the pressure-strain correlation of turbulence: an invariant dyanmic systems approach. *J. Fluid Mech.* **227**, 245–272.

- SUTERA, S. P. 1965 Vorticity amplification in stagnation-point flow and its effect on heat transfer. *J. Fluid Mech.* **21**, 513–534.
- THEOFILIS, V., FEDOROV, A., OBRIST, D. & DALLMANN, U. C. 2003 The extended Görtler-Hämmerlin model for linear instability of three-dimensional incompressible swept attachment-line boundary layer flow. *J. Fluid Mech.* **487**, 271–313.
- VAN FOSSEN, G. J., SIMONEAU, R. J. & CHING, C. Y. 1995 Influence of turbulence parameters, Reynolds number and body shape on stagnation region heat transfer. *ASME Journal of Heat Transfer* **117**, 593–603.
- WILCOX, D. C. 2001 Turbulence modeling: An overview. *AIAA Paper 2001-0724* .
- WILSON, S. D. R. & GLADWELL, I. 1978 The stability of a two-dimensional stagnation flow to three-dimensional disturbances. *J. Fluid Mech.* **84**, 517–527.
- WLEZIEN, R. W. 1994 Measurement of acoustic receptivity. *25th AIAA Fluid Dynamics Conference, AIAA 94-2221* .
- XIONG, Z. 2004 Stagnation point flow and heat transfer under free-stream turbulence. PhD thesis, Stanford University.
- XIONG, Z. & LELE, S. K. 2001 Numerical study of leading-edge heat transfer under free-stream turbulence. *AIAA Paper 2001-1016* .
- XIONG, Z. & LELE, S. K. 2004 Distortion of upstream disturbances in a Hiemenz boundary layer. *J. Fluid Mech.* **519**, 201–232.
- XIONG, Z., NAGARAJAN, S. & LELE, S. K. 2004 Simple method for generating inflow turbulence. *AIAA Journal* **42** (10), 2164–2166.